Journal of Computational Physics 488 (2023) 112216

Contents lists available at ScienceDirect

Journal of Computational Physics

journal homepage: www.elsevier.com/locate/jcp

Modified diffuse interface fluid model and its consistent energy-stable computation in arbitrary domains

Junxiang Yang [a], Zhijun Tan [a,b], Jian Wang [c,d,e], Junseok Kim [f,*]

[a] School of Computer Science and Engineering, Sun Yat-sen University, Guangzhou 510006, China
[b] Guangdong Province Key Laboratory of Computational Science, Sun Yat-sen University, Guangzhou 510275, China
[c] School of Mathematics and Statistics, Nanjing University of Information Science and Technology, Nanjing, 210044, China
[d] Center for Applied Mathematics of Jiangsu Province, Nanjing University of Information Science and Technology, Nanjing, 210044, China
[e] Jiangsu International Joint Laboratory on System Modeling and Data Analysis, Nanjing University of Information Science and Technology, Nanjing, 210044, China
[f] Department of Mathematics, Korea University, Seoul, 02841, Republic of Korea

ARTICLE INFO

Article history:
Received 3 January 2023
Received in revised form 1 May 2023
Accepted 2 May 2023
Available online 8 May 2023

Keywords:
Binary fluid system
Arbitrary domain
Energy-stable method
Contact angle condition

ABSTRACT

Binary fluid flows in irregular domains are common phenomena in natural and industrial fields. To describe these physical processes, we herein present a novel fluid flow-coupled two-material model reflecting different wetting conditions on an arbitrary fluid-solid interface. A modified ternary Cahn–Hilliard (CH) diffuse interface model is adopted to capture the fluid-fluid interface. One of three components is fixed for all time to represent the profile of complex domains. By considering the contact angle condition on solid-fluid interface and equilibrium interface assumption, an extra wetting term is derived. To treat the fluid flow in domains with solid obstacles, we consider the entire system as a porous medium with variable permeability and add a large penalty term into the incompressible Navier–Stokes (NS) equations. It can be proven that the proposed modified Cahn–Hilliard–Navier–Stokes (CHNS) system satisfies the energy dissipation law (energy stability). Based on the scalar auxiliary variable (SAV) approach with appropriate correction techniques, the linear and consistent energy-stable scheme is developed. We introduce the numerical implementation and estimate the discrete version of energy stability in detail. The proposed method can be implemented on regular Cartesian grids with the absence of explicit boundary treatment. Moreover, the calculations are totally decoupled in each time step. Extensive numerical experiments not only indicate the expected accuracy and stability but also show the superior performance in arbitrary domains with different wetting conditions.

1. Introduction

In industrial or natural field, most domains of binary fluid flows are irregular. For example, the formation of liquid jet in a flow focusing instrument [1,2], the vesicle in blood vessel or micro-fluid device [3,4], flows in porous medium [5], and tissue growth in culture dish [6], etc. In these irregular domains, the binary fluid flows generally undergo complex change

* Corresponding author.
E-mail address: cfdkim@korea.ac.kr (J. Kim).
URL: https://mathematicians.korea.ac.kr/cfdkim/ (J. Kim).

https://doi.org/10.1016/j.jcp.2023.112216
0021-9991/

of interface, such as breakage, coalescence, and deformation. To efficiently and practically capture the topological changes of two-material interfaces, the diffuse interface (phase-field) method is a popular approach in which one or several order parameters (phase functions) are used to represent the volume fractions of different fluid components. The interface can be implicitly obtained by solving the governing equations of the order parameters, see [7–10] for the successful applications of the diffuse interface method in multi-component fluid simulations.

In the diffuse interface method, the Cahn–Hilliard (CH) equation [11] is commonly used to capture the fluid interface because of its natural property of mass conservation. Furthermore, the CH equation is thermodynamically consistent, i.e., the free energy of system satisfies a dissipation law when appropriate boundary conditions (periodic or homogeneous-Neumann) are considered. On the numerical level, the energy dissipation-preserving computation not only maintains the consistency with physical property but also prevents some unwanted numerical oscillations. Therefore, many researchers have developed and investigated energy-stable numerical methods for the CH equation, such as the nonlinear convex splitting scheme [12,13], stabilization-type method [14,15], auxiliary variable-type method [16–18], and exponential time differencing method [19], etc. However, most of these works focus on the problems either in regular domain or without wetting condition.

For the binary fluid flows in an arbitrary domain, the wetting condition should be considered because the fluid phase can contact with solid. To model this problem, Luo et al. [20] applied the finite element method (FEM) to directly discretize the computational domains with complex shapes and imposed appropriate wetting condition on each boundary point. Compared with the direct FEM on treating complex domain, the embedded domain-type method is more efficient. The basic idea of this method is to represent the profile of solid region with a specific level set of phase function which is defined inside a larger regular domain. On the boundary of regular domain, we still use simple boundary treatment, such as the periodic or zero Neumann boundary condition. The wetting condition on fluid-solid boundary is implicitly satisfied by solving the governing equations. Li et al. [21] presented a CH-type model by recasting the classical ternary system and added a wetting term based on the geometrical assumption. Their proposed model was solved by a first-order linear splitting method and adaptive mesh refinement. Similar ideas of embedded domain can also be found in [22] for quasi-incompressible binary flows in contact with solid obstacles. In a recent work of Yang et al. [23], a temporally second-order accurate and energy-stable linear method was proposed for treating the modified CH model in arbitrary domains. It is worth noting that the modified model [21,23] is based on the following ternary CH system [24,25]

$$\frac{\partial \phi_i}{\partial t} = \frac{1}{Pe}\Delta \mu_i, \tag{1.1}$$

$$\mu_i = F'(\phi_i) + \beta(\boldsymbol{\phi}) - \epsilon^2 \Delta \phi_i, \quad i = 0, 1, 2, \tag{1.2}$$

where ϕ_i is the order parameter of i-th component, μ_i is the chemical potential, Pe is the Peclect number related to mobility, ϵ is a parameter. The nonlinear term is $F'(\phi_i) = \phi_i^3 - \phi_i$. The Lagrange multiplier $\beta(\boldsymbol{\phi})$ is used to satisfy the link condition, i.e., $\phi_0 + \phi_1 + \phi_2 = 1$ [24,25]. For successful numerical methods and applications of the ternary CH model, see [26–29] and references therein.

The present study aims to develop a novel diffuse interface-type model for incompressible binary fluid flows with wetting condition in arbitrary domains. Based on the modified version of the ternary CH model, geometrical contact angle relation, and equilibrium interface assumption, the governing equations are derived to capture the binary fluid interface. The wetting condition on fluid-solid boundary is implicitly achieved by solving the equations without explicit boundary treatment. To describe the fluid flows in the domain with solid wall or obstacles, a penalty term is introduced into the incompressible Navier–Stokes (NS) equations. After each computation, the velocity evolution inside the solid phase is effectively suppressed. The whole system can be easily implemented on Cartesian grids. Moreover, the energy dissipation law of the proposed model can be analytically estimated. Based on an auxiliary variable-type method with correction techniques, the linear, temporally second-order, and unconditionally energy-stable method is developed. The proposed scheme can be implemented in a totally decoupled manner and still satisfies the time-discretized energy dissipation law. To the best of our knowledge, this is the first study focusing on a Cartesian grid based diffuse interface fluid model with wetting condition in complex domains and its consistent energy-stable computation. Theoretically, any discretization methods in space can be directly used on this model.

The rest parts are organized as follows. In Section 2, we present the governing equations for describing binary flows in complex domains. In Section 3, the linear energy-stable method and the detailed implementation are introduced. Extensive computational tests are shown in Section 4. The conclusions are drawn in Section 5.

2. Proposed model in arbitrary domain

In present work, we fix one component (i.e., ϕ_0) in the ternary CH model for all time and use its 0.5 level set to represent the profile of solid domain. We let $\phi_0 = 1$ and 0 in the interior and exterior of solid, respectively. In the exterior of solid, the region is occupied by fluid phases, i.e., ϕ_1 and ϕ_2. From the link condition, i.e., $\phi_0 + \phi_1 + \phi_2 = 1$, we know that the fluid and solid can not penetrate into the bulk phase of each other.

When we consider the binary fluid system in contact with solid, the wetting condition should be reflected because the real solid surface generally has hydrophobic or hydrophilic property. From the perspective of physics, the wetting condition

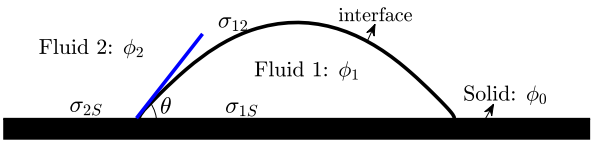

Fig. 1. Schematic illustration of a droplet in contact with solid. Here, θ is the contact angle. The surface tensions are σ_{12}, σ_{1S}, and σ_{2S}.

can be approximately described by the dihedral contact angle among fluid and solid phases. Moreover, the Young's equality [21] gives the relation between surface tensions and contact angle, i.e.,

$$\sigma_{12}\cos\theta = \sigma_{2S} - \sigma_{1S}, \tag{2.1}$$

where θ is the contact angle, σ_{12}, σ_{1S}, and σ_{2S} are the surface tensions on the interfaces between fluid 1 and fluid 2, fluid 1 and solid, fluid 2 and solid. A schematic illustration of single droplet in contact with solid substrate is shown in Fig. 1.

Based on the local equilibrium interface assumption [24], the relation $|\nabla\phi_i| = \phi_i(1-\phi_i)/(\sqrt{2}\epsilon)$ holds. Because ϕ_0 is used to represent the solid and ϕ_i is the fluid, we have the following boundary condition on fluid-solid boundary

$$\nabla\phi_i \cdot \mathbf{n}_S = -|\nabla\phi_i|\cos\theta_i = -\phi_i(1-\phi_i)\cos\theta_i/(\sqrt{2}\epsilon), \tag{2.2}$$

where $\theta_i = 180^\circ - \theta$ and $\mathbf{n}_S = \nabla\phi_0/|\nabla\phi_0|$ is the unit normal vector to fluid-solid boundary. Now, we recast Eq. (2.2) to be

$$\epsilon^2\nabla\phi_0\cdot\nabla\phi_i + \epsilon\phi_i(1-\phi_i)|\nabla\phi_0|\cos\theta_i/\sqrt{2} = 0. \tag{2.3}$$

By adding the above "zero-contribution" equality into the original chemical potential, we have

$$\mu_i = F'(\phi_i) + \beta(\phi_i) + \epsilon\phi_i(1-\phi_i)|\nabla\phi_0|\cos\theta_i/\sqrt{2} - \epsilon^2\nabla\cdot((1-\phi_0)\nabla\phi_i) - \epsilon^2\phi_0\Delta\phi_i. \tag{2.4}$$

Here, $\Delta\phi_i = \nabla\cdot((1-\phi_0)\nabla\phi_i) + \nabla\phi_0\cdot\nabla\phi_i + \phi_0\Delta\phi_i$ is used. It is worth noting that the above equation and original chemical potential are equivalent in fluid region because $\phi_0 = 0$. On the fluid-solid boundary, the last term in Eq. (2.4) becomes zero as $\phi_0 \to 0$. Moreover, we notice that the last term does not contain the contact angle. By imposing strict restriction on the evolution in solid and ignoring the effect of last term in Eq. (2.4) on fluid-solid boundary, we derive the following modified model in an arbitrary domain

$$\frac{\partial\phi_i}{\partial t} = \frac{1}{Pe}\nabla\cdot((1-\phi_0)\nabla\mu_i), \tag{2.5}$$

$$\mu_i = F'(\phi_i) + \beta(\boldsymbol{\phi}) + \frac{\epsilon}{\sqrt{2}}\phi_i(1-\phi_i)|\nabla\phi_0|\cos\theta_i - \epsilon^2\nabla\cdot((1-\phi_0)\nabla\phi_i), \quad i = 1,2. \tag{2.6}$$

Here, we note $\theta_2 = 180^\circ - \theta_1$. Based on the above model, the arbitrary solid region is actually embedded into a larger regular domain Ω. On the regular domain boundary $\partial\Omega$, the periodic or the homogeneous-Neumann boundary condition (i.e., $\nabla\phi_i\cdot\mathbf{n}|_{\partial\Omega} = 0$ and $\nabla\mu_i\cdot\mathbf{n}|_{\partial\Omega} = 0$, $i = 0, 1, 2$) is considered. Inspired by [24–26], the similar form of $\beta(\boldsymbol{\phi})$ is defined as

$$\beta(\boldsymbol{\phi}) = -\frac{1}{3}\left[\sum_{i=1}^{2}\left(F'(\phi_i) + \epsilon\phi_i(1-\phi_i)|\nabla\phi_0|\cos\theta_i/\sqrt{2}\right) + F'(\phi_0)\right].$$

For the solid phase, the contact angle is absent and we only consider the effect of $F'(\phi_0)$ in above equality. Equations (2.5) and (2.6) can be used to capture the fluid-fluid interface in an arbitrary domain and the interface is represented by the 0.5 level set of ϕ_i. To model the hydrodynamics coupled binary materials in the domain with fixed solid wall or obstacles, a basic fact is to suppress the velocity field in solid phase. In our work, we aim to propose a Cartesian grid-based model satisfying the energy dissipation law. Based on the penalty idea in Bergmann et al. [30], the dimensionless incompressible NS equations with constant density and viscosity are written to be

$$\frac{\partial\mathbf{u}}{\partial t} + \mathbf{u}\cdot\nabla\mathbf{u} = -\nabla p + \frac{1}{Re}\Delta\mathbf{u} - \frac{1}{We}\sum_{i=1}^{2}\phi_i\nabla\mu_i + \frac{\phi_0}{\kappa}(\mathbf{u}_S - \mathbf{u}), \tag{2.7}$$

$$\nabla\cdot\mathbf{u} = 0, \tag{2.8}$$

where $\mathbf{u} = (u, v)$ or $\mathbf{u} = (u, v, w)$ is the velocity field. The velocity of solid is $\mathbf{u}_S$. The pressure is p and the third term on the right-hand side reflects the effect of surface tension. The dimensionless numbers are Reynolds number Re and Weber number We, see [24–27] for detailed definitions. The last term on the right-hand side is the penalty term which suppresses the velocity field in solid. The permeability κ is a constant and $0 < \kappa \ll 1$. Because we assume the solid phase is fixed, $\mathbf{u}_S$ is zero in this work and we have the following particular equations

$$\frac{\partial \mathbf{u}}{\partial t} + \mathbf{u}\cdot\nabla\mathbf{u} = -\nabla p + \frac{1}{Re}\Delta\mathbf{u} - \frac{1}{We}\sum_{i=1}^{2}\phi_i\nabla\mu_i - \frac{\phi_0}{\kappa}\mathbf{u}, \tag{2.9}$$

$$\nabla\cdot\mathbf{u} = 0. \tag{2.10}$$

By adding the convection effect into the phase-field model, the modified CHNS system for binary incompressible flows in an arbitrary domain is postulated as

$$\frac{\partial \phi_i}{\partial t} + \nabla\cdot(\mathbf{u}\phi_i) = \frac{1}{Pe}\nabla\cdot((1-\phi_0)\nabla\mu_i), \tag{2.11}$$

$$\mu_i = F'(\phi_i) + \beta(\boldsymbol{\phi}) + \epsilon\phi_i(1-\phi_i)|\nabla\phi_0|\cos\theta_i/\sqrt{2} - \epsilon^2\nabla\cdot((1-\phi_0)\nabla\phi_i), \quad i=1,2, \tag{2.12}$$

$$\frac{\partial \mathbf{u}}{\partial t} + \mathbf{u}\cdot\nabla\mathbf{u} = -\nabla p + \frac{1}{Re}\Delta\mathbf{u} - \frac{1}{We}\sum_{i=1}^{2}\phi_i\nabla\mu_i - \frac{\phi_0}{\kappa}\mathbf{u}, \tag{2.13}$$

$$\nabla\cdot\mathbf{u} = 0. \tag{2.14}$$

On the domain boundaries, the periodic boundary condition or $\mathbf{u}=0$ is used for velocity field. Before the start of the following contents, we define some useful notations. Let f_a and f_b be two integrable functions, the L^2-inner product is defined as $(f_a, f_b) = \int_\Omega f_a\cdot f_b\, d\mathbf{x}$, the L^2-norm is defined as $\|f_a\|^2 = (f_a, f_a)$. By multiplying $\mathbf{1}$ on Eq. (2.11) and utilizing the divergence theorem and appropriate boundary condition, it is easy to check that ϕ_i is mass-conserved, i.e., $\frac{d}{dt}\int_\Omega \phi_i\, d\mathbf{x} = 0$. Furthermore, the proposed system, i.e., Eqs. (2.11)–(2.14), satisfy the following theorem.

Theorem 2.1. *The solutions of Eqs. (2.11)–(2.14) dissipate a total energy functional as follows*

$$E_o = \int_\Omega \sum_{i=1}^{2}\left[\frac{\epsilon^2}{2}(1-\phi_0)|\nabla\phi_i|^2 + F(\phi_i) + \epsilon\left(\frac{\phi_i^2}{2} - \frac{\phi_i^3}{3}\right)|\nabla\phi_0|\cos\theta_i\right] d\mathbf{x} + \int_\Omega \frac{We}{2}|\mathbf{u}|^2\, d\mathbf{x}. \tag{2.15}$$

Proof. By multiplying Eq. (2.11) with μ_i and taking the L^2-inner product, we get

$$\left(\frac{\partial\phi_i}{\partial t}, \mu_i\right) + (\nabla\cdot(\mathbf{u}\phi_i), \mu_i) = -\frac{1}{Pe}\|\sqrt{1-\phi_0}\nabla\mu_i\|^2, \tag{2.16}$$

where the integral by parts and appropriate boundary condition (periodic or homogeneous-Neumann type) are used. By multiplying Eq. (2.12) with $\partial\phi_i/\partial t$ and taking the L^2-inner product, we have

$$\begin{aligned}\left(\mu_i, \frac{\partial\phi_i}{\partial t}\right) = \frac{d}{dt}\int_\Omega F(\phi_i)\, d\mathbf{x} + \left(\beta(\boldsymbol{\phi}), \frac{\partial\phi_i}{\partial t}\right) + \frac{d}{dt}\int_\Omega \epsilon\left(\frac{\phi_i^2}{2} - \frac{\phi_i^3}{3}\right)|\nabla\phi_0|\cos\theta_i\, d\mathbf{x} \\ + \frac{d}{dt}\int_\Omega \frac{\epsilon^2}{2}(1-\phi_0)|\nabla\phi_i|^2\, d\mathbf{x}.\end{aligned} \tag{2.17}$$

By taking the L^2-inner product of Eq. (2.13) with $We\mathbf{u}$, we have

$$\frac{d}{dt}\int_\Omega \frac{We}{2}|\mathbf{u}|^2\, d\mathbf{x} = -\frac{We}{Re}\|\nabla\mathbf{u}\|^2 - \frac{We}{\kappa}\|\sqrt{\phi_0}\mathbf{u}\|^2 + (\phi_1\nabla\mu_1 + \phi_2\nabla\mu_2, \mathbf{u}), \tag{2.18}$$

where $(\mathbf{u}\cdot\nabla\mathbf{u}, \mathbf{u}) = 0$ and $(-\nabla p, \mathbf{u}) = 0$ [31,32] are used. By combining Eq. (2.18) with Eqs. (2.16)–(2.17) from $i=1$ to 2, we obtain

$$\frac{d}{dt}E_o = -\frac{We}{Re}\|\nabla\mathbf{u}\|^2 - \frac{We}{\kappa}\|\sqrt{\phi_0}\mathbf{u}\|^2 - \frac{1}{Pe}\sum_{i=1}^{2}\|\sqrt{1-\phi_0}\nabla\mu_i\|^2 \le 0, \tag{2.19}$$

where $\left(\beta(\boldsymbol{\phi}), \frac{\partial(\phi_1+\phi_2)}{\partial t}\right) = \left(\beta(\boldsymbol{\phi}), \frac{\partial(1-\phi_0)}{\partial t}\right) = 0$ is used because ϕ_0 is constant with respect to time t. The above inequality completes the proof. □

Theorem 2.2. *The proposed model satisfies the mass conservation of ϕ_i.*

Proof. By taking the integral on both sides of Eq. (2.11), we have

$$\int_\Omega \frac{\partial \phi_i}{\partial t}\, d\mathbf{x} = \frac{d}{dt}\int_\Omega \phi_i\, d\mathbf{x} = -\int_\Omega \nabla\cdot(\mathbf{u}\phi_i)\, d\mathbf{x} + \frac{1}{Pe}\int_\Omega \nabla\cdot((1-\phi_0)\nabla\mu_i)\, d\mathbf{x}$$
$$= \frac{1}{Pe}\int_{\partial\Omega}(1-\phi_0)\nabla\mu_i\cdot\mathbf{n}\, ds = 0, \tag{2.20}$$

where the divergence theorem, $\mathbf{u}|_{\partial\Omega}=0$, and $\nabla\mu_i\cdot\mathbf{n}|_{\partial\Omega}=0$ are used. The aforementioned result indicates that $\int_\Omega \phi_i\, d\mathbf{x}$ is conserved. The proof is completed. □

3. Computational solution algorithm

Now, we first derive the equivalent equations by introducing time-dependent auxiliary variables. The equivalent form is essential to develop linearly decoupled, second-order time-accurate, and energy-stable method. Later, we describe the time-marching method based on second-order backward difference formula (BDF2) and present its energy stability and totally decoupled implementation.

3.1. Equivalent equations

The SAV method was originally presented by Shen et al. [33] to construct linear energy-stable schemes for the gradient flows. Because the difficulty of energy estimation mainly comes from the nonlinear terms, the basic idea of SAV method is to introduce a time-dependent auxiliary variable which is related to the nonlinear terms. By performing the time derivative to the auxiliary variable, an extra evolutional equation can be obtained to complete the system. In this context, the energy stability can be easily proved since the inner products of nonlinear terms and the right-hand side of extra evolutional equation balance themselves out. Based on the similar idea, Lin et al. [34] developed a SAV-type numerical approximation for the incompressible NS equations. With $\mathbf{u}|_{\partial\Omega}=0$ and divergence-free condition, we have $(\mathbf{u}\cdot\nabla\mathbf{u},\mathbf{u})=0$ and $(\nabla\cdot(\mathbf{u}\phi_i),\mu_i)+(\phi_i\nabla\mu_i,\mathbf{u})=0$. Because there terms are "zero-energy-contribution", we can introduce an auxiliary variable $\equiv 1$, then its time derivative equals to zero. Based on the similar treatment of SAV method, the difficulty resulting from nonlinear and coupled terms can be eliminated in energy estimation. Please refer to [35,36] for some successful applications. To construct equivalent equations, we define $r(t)$ and $q(t)$:

$$r = r(t) = \sqrt{\int_\Omega \sum_{i=1}^{2}\left[F(\phi_i) + \epsilon\left(\frac{\phi_i^2}{2}-\frac{\phi_i^3}{3}\right)|\nabla\phi_0|\cos\theta_i/\sqrt{2}\right] d\mathbf{x} + B}, \tag{3.1}$$

$$q = q(t) = 1, \quad \frac{dq}{dt} = 0, \tag{3.2}$$

where B is a large enough constant to ensure the positivity. Equations (2.11)–(2.14) are recast to be the following equivalent forms

$$\frac{\partial\phi_i}{\partial t} + q\nabla\cdot(\mathbf{u}\phi_i) = \frac{1}{Pe}\nabla\cdot((1-\phi_0)\nabla\mu_i), \tag{3.3}$$

$$\mu_i = r\left(H_i + \tilde{\beta}(\boldsymbol{\phi})\right) - \epsilon^2\nabla\cdot((1-\phi_0)\nabla\phi_i), \tag{3.4}$$

$$\frac{\partial\mathbf{u}}{\partial t} + q\mathbf{u}\cdot\nabla\mathbf{u} = -\nabla p + \frac{1}{Re}\Delta\mathbf{u} - \frac{q}{We}\sum_{i=1}^{2}\phi_i\nabla\mu_i - \frac{\phi_0}{\kappa}\mathbf{u}, \tag{3.5}$$

$$\nabla\cdot\mathbf{u} = 0, \tag{3.6}$$

$$\frac{dr}{dt} = \frac{1}{2}\int_\Omega \sum_{i=1}^{2} H_i\frac{\partial\phi_i}{\partial t}\, d\mathbf{x}, \tag{3.7}$$

$$\frac{dq}{dt} = \int_\Omega\left(\sum_{i=1}^{2}[\nabla\cdot(\mathbf{u}\phi_i)\mu_i + \phi_i\nabla\mu_i\cdot\mathbf{u}] + We\mathbf{u}\cdot\nabla\mathbf{u}\cdot\mathbf{u}\right) d\mathbf{x}. \tag{3.8}$$

Here,

$$H_i = \frac{F'(\phi_i) + \epsilon\phi_i(1-\phi_i)|\nabla\phi_0|\cos\theta_i/\sqrt{2}}{\sqrt{\int_\Omega \sum_{i=1}^{2}\left[F(\phi_i) + \epsilon\left(\frac{\phi_i^2}{2} - \frac{\phi_i^3}{3}\right)|\nabla\phi_0|\cos\theta_i/\sqrt{2}\right] d\mathbf{x} + B}},$$

$$\tilde{\beta}(\boldsymbol{\phi}) = -\frac{1}{3}\left[\sum_{i=1}^{2} H_i + \frac{F'(\phi_0)}{\sqrt{\int_\Omega \sum_{i=1}^{2}\left[F(\phi_i) + \epsilon\left(\frac{\phi_i^2}{2} - \frac{\phi_i^3}{3}\right)|\nabla\phi_0|\cos\theta_i/\sqrt{2}\right] d\mathbf{x} + B}}\right].$$

The same boundary conditions in previous section are used. Because we introduce two extra variables: r and q, Eqs. (3.7) and (3.8) provide two evolutional equations of r and q to complete the calculations. Following the estimations in [32], it is simple to check the right-hand side of Eq. (3.8) is zero. Thus, Eq. (3.8) satisfies the definition of dq/dt in Eq. (3.2). From the definitions of r and q, it can be observed that Eqs. (3.3)–(3.6) and Eqs. (2.11)–(2.12) are indeed equivalent. By using the similar estimations in previous section, the energy dissipation law holds with respect to the following equivalent energy

$$E_o^e = |r|^2 + \int_\Omega \sum_{i=1}^{2}\left(\frac{\epsilon^2}{2}(1-\phi_0)|\nabla\phi_i|^2\right) d\mathbf{x} + \int_\Omega \frac{We}{2}|\mathbf{u}|^2\, d\mathbf{x} - B. \tag{3.9}$$

Remark 3.1. To estimate an appropriate value of B, we only need to consider $\left[\epsilon\left(\frac{\phi_i^2}{2} - \frac{\phi_i^3}{3}\right)|\nabla\phi_0|\cos\theta_i/\sqrt{2}\right]$ because $F(\phi_i)$ is non-negative. From [37], we define ϵ as $\epsilon = \epsilon_l = lh/(4\sqrt{2}\tanh^{-1}(0.9))$ which indicates the diffuse interface approximately occupies l spatial grids. The spatial step is h and it will be defined in subsection 3.4. If we consider a central difference stencil to approximate $|\nabla\phi_0|$ in space, a 1D example is $|\nabla\phi_0| = |(\phi_0(x_{m+1}) - \phi_0(x_{m-1}))/(2h)|$. Then, we have

$$\epsilon\left(\frac{\phi_i^2}{2} - \frac{\phi_i^3}{3}\right)|\nabla\phi_0|\cos\theta_i/\sqrt{2} \approx \frac{lh}{8\tanh^{-1}(0.9)}\left(\frac{\phi_i^2}{2} - \frac{\phi_i^3}{3}\right)\left|\frac{\phi_0(x_{m+1}) - \phi_0(x_{m-1})}{2h}\right|\cos\theta_i.$$

Although the CH dynamics will causes the numerical value of ϕ_i slightly overflows $[0, 1]$, the value of $\left(\frac{\phi_i^2}{2} - \frac{\phi_i^3}{3}\right)$ is non-negative even if $\phi_i \in [-0.5, 1.5]$. In this context, we have

$$0 \le \left(\frac{\phi_i^2}{2} - \frac{\phi_i^3}{3}\right) \le 0.1667 \ \text{ for } \ \phi_i \in [-0.5, 1.5].$$

As $\cos\theta_i = 1$, $\int_\Omega \sum_{i=1}^{2}\left[\epsilon\left(\frac{\phi_i^2}{2} - \frac{\phi_i^3}{3}\right)|\nabla\phi_0|\cos\theta_i/\sqrt{2}\right] d\mathbf{x}$ will be non-negative. As $\cos\theta_i = -1$, we get

$$\epsilon\left(\frac{\phi_i^2}{2} - \frac{\phi_i^3}{3}\right)|\nabla\phi_0|\cos\theta_i/\sqrt{2} \ge -\frac{0.1667l}{16\tanh^{-1}(0.9)},$$

where $|(\phi_0(x_{m+1}) - \phi_0(x_{m-1}))/(2h)| \le 1/(2h)$ is used. Then, we get

$$\int_\Omega \sum_{i=1}^{2}\left[\epsilon\left(\frac{\phi_i^2}{2} - \frac{\phi_i^3}{3}\right)|\nabla\phi_0|\cos\theta_i/\sqrt{2}\right] d\mathbf{x} \ge -\frac{0.1667l}{8\tanh^{-1}(0.9)}|\Omega|,$$

where $|\Omega|$ is the area of computational domain. We can approximately set $B > \frac{0.1667l}{8\tanh^{-1}(0.9)}|\Omega|$. In actual simulation, B can take a small enough value because ϕ_i is almost bounded by 0 and 1.

3.2. Temporally second-order accurate scheme

Let T be the computational time and N^T be the number of time iteration, the uniform time step is defined as $\Delta t = T/N^T$. For each variable, we define $(\cdot)^n$ as the numerical approximation at n-th time level. Based on BDF2, the proposed scheme contains three steps in each time step.

Step 1. With computed variables at previous time levels, we update ϕ_i^{n+1}, $\mathbf{u}^{n+1}$, and p^{n+1} by

$$\frac{3\phi_i^{n+1}-4\phi_i^n+\phi_i^{n-1}}{2\Delta t}+\hat{q}^{n+1}\nabla\cdot(\mathbf{u}^*\phi_i^*)=\frac{1}{Pe}\nabla\cdot((1-\phi_0)\nabla\mu_i^{n+1}), \tag{3.10}$$

$$\mu_i^{n+1}=\hat{r}^{n+1}\left(H_i^*+\beta(\boldsymbol{\phi}^*)\right)-\epsilon^2\nabla\cdot\left((1-\phi_0)\nabla\phi_i^{n+1}\right)+S(\phi_i^{n+1}-\phi_i^*),\ \ i=1,2, \tag{3.11}$$

$$\frac{3\tilde{\mathbf{u}}^{n+1}-4\mathbf{u}^n+\mathbf{u}^{n-1}}{2\Delta t}+\hat{q}^{n+1}\mathbf{u}^*\cdot\nabla\mathbf{u}^*=-\nabla p^n+\frac{1}{Re}\Delta\tilde{\mathbf{u}}^{n+1}-\frac{\hat{q}^{n+1}}{We}\sum_{i=1}^{2}\phi_i^*\nabla\mu_i^*-\frac{\phi_0}{\kappa}\tilde{\mathbf{u}}^{n+1}, \tag{3.12}$$

$$\frac{3\mathbf{u}^{n+1}-3\tilde{\mathbf{u}}^{n+1}}{2\Delta t}=-\left(\nabla p^{n+1}-\nabla p^n\right), \tag{3.13}$$

$$\nabla\cdot\mathbf{u}^{n+1}=0, \tag{3.14}$$

$$3\hat{r}^{n+1}-4r^n+r^{n-1}=\frac{1}{2}\int_\Omega\sum_{i=1}^{2}H_i^*(3\phi_i^{n+1}-4\phi_i^n+\phi_i^{n-1})\,d\mathbf{x}, \tag{3.15}$$

$$\frac{3\hat{q}^{n+1}-4q^n+q^{n-1}}{2\Delta t}=\int_\Omega\left(\sum_{i=1}^{2}\left[\nabla\cdot(\mathbf{u}^*\phi_i^*)\mu_i^{n+1}+\phi_i^*\nabla\mu_i^*\cdot\tilde{\mathbf{u}}^{n+1}\right]+We\mathbf{u}^*\cdot\nabla\mathbf{u}^*\cdot\tilde{\mathbf{u}}^{n+1}\right)d\mathbf{x}, \tag{3.16}$$

where $(\cdot)^*=2(\cdot)^n-(\cdot)^{n-1}$ and $S>0$ is a stabilization constant. On the boundaries of regular domain Ω, the periodic or the following boundary conditions are used

$$\mathbf{u}^{n+1}\cdot\mathbf{n}|_{\partial\Omega}=0,\ \tilde{\mathbf{u}}^{n+1}|_{\partial\Omega}=0,\ \nabla\phi_i^{n+1}\cdot\mathbf{n}|_{\partial\Omega}=\nabla\mu_i^{n+1}\cdot\mathbf{n}|_{\partial\Omega}=0,\ \nabla p^{n+1}\cdot\mathbf{n}|_{\partial\Omega}=\nabla p^n\cdot\mathbf{n}|_{\partial\Omega}=0.$$

In above equations, the calculated $\hat{r}^{n+1}$ and $\hat{q}^{n+1}$ are not equal to their definitions in general. When a larger time step is used, these differences will become more obvious and then the consistency between numerical method and equivalent equations is lost. To improve the consistency for r, Jiang et al. [38] recently developed a simple and practical correction algorithm after each computation. To facilitate the interested readers, we still describe this correction technique in Step 2. Moreover, we also develop a new correction technique for q in Step 3 to further improve the consistency.

Step 2. With computed $\hat{r}^{n+1}$ and ϕ_i^{n+1}, we obtain r^{n+1} with the following correction

$$r^{n+1}=\xi_o\hat{r}^{n+1}+(1-\xi_o)J(\phi_i^{n+1}), \tag{3.17}$$

where

$$J(\phi_i)=\sqrt{\int_\Omega\sum_{i=1}^{2}\left[F(\phi_i)+\epsilon\left(\frac{\phi_i^2}{2}-\frac{\phi_i^3}{3}\right)|\nabla\phi_0|\cos\theta_i/\sqrt{2}\right]d\mathbf{x}+B}.$$

Here, $\xi_o=\min\limits_{\xi\in[0,1]}\xi$ such that

$$\frac{1}{2}(|r^{n+1}|^2+|2r^{n+1}-r^n|^2)-\frac{1}{2}(|\hat{r}^{n+1}|^2+|2\hat{r}^{n+1}-r^n|^2)\le\Delta t\eta_1\sum_{i=1}^{2}\|\sqrt{1-\phi_0}\nabla\mu_i^{n+1}\|^2, \tag{3.18}$$

where $0<\eta_1\le\frac{1}{Pe}$. Actually, the above inequality can be simplified as

$$a\xi^2+b\xi+c\le0, \tag{3.19}$$

where

$$a=\frac{5}{2}\left(\hat{r}^{n+1}-J(\phi_i^{n+1})\right)^2,\quad b=\left(\hat{r}^{n+1}-J(\phi_i^{n+1})\right)\left(5J(\phi_i^{n+1})-2r^n\right),$$

$$c=\frac{1}{2}\left(|J(\phi_i^{n+1})|^2+|2J(\phi_i^{n+1})-r^n|^2-|\hat{r}^{n+1}|^2-|2\hat{r}^{n+1}-r^n|^2\right)-\Delta t\eta_1\sum_{i=1}^{2}\|\sqrt{1-\phi_0}\nabla\mu_i^{n+1}\|^2.$$

It is worth noting that $a+b+c\le0$. With $a\neq0$, we have

$$\xi_o=\max\{0,\ \left(-b-\sqrt{b^2-4ac}\right)/(2a)\}. \tag{3.20}$$

If $a=0$, then the correction is not necessary. Some details of this correction technique can be found in [38].

Step 3. With computed $\hat{q}^{n+1}$ and $\tilde{\mathbf{u}}^{n+1}$, we obtain q^{n+1} with the following correction

$$q^{n+1} = \chi_o \hat{q}^{n+1} + (1 - \chi_o). \tag{3.21}$$

Here, $\chi_o = \min_{\chi \in [0,1]} \chi$ such that

$$\frac{1}{2}\left(|q^{n+1}|^2 + |2q^{n+1} - q^n|^2\right) - \frac{1}{2}\left(|\hat{q}^{n+1}|^2 + |2\hat{q}^{n+1} - q^n|^2\right) \le \Delta t \eta_2 \left(\|\nabla \tilde{\mathbf{u}}^{n+1}\|^2 + \|\sqrt{\phi_0}\tilde{\mathbf{u}}^{n+1}\|^2\right), \tag{3.22}$$

where $0 < \eta_2 \le \min\{\frac{2We}{Re}, \frac{2We}{\kappa}\}$. The above inequality can be simplified as

$$d\chi^2 + e\chi + f \le 0, \tag{3.23}$$

where

$$d = 5\left(\hat{q}^{n+1} - 1\right)^2, \quad e = 4(q^n - 1)(1 - \hat{q}^{n+1}),$$
$$f = 5 - |q^n|^2 - 4q^n - \Delta t \eta_2 \left(\|\nabla \tilde{\mathbf{u}}^{n+1}\|^2 + \|\sqrt{\phi_0}\tilde{\mathbf{u}}^{n+1}\|^2\right).$$

We notice that $d + e + f \le 0$. With $d \ne 0$, we have

$$\chi_o = \max\{0, \left(-e - \sqrt{e^2 - 4df}\right)/(2d)\}. \tag{3.24}$$

When $d = 0$, the correction is not necessary. After the corrections in Step 2 and Step 3, the updated values: r^{n+1} and q^{n+1} are more consistent with their definitions. In each time step, we perform Steps 1-3 in a step-by-step manner to obtain the solutions.

Theorem 3.1. *The solutions in Steps 1-3 dissipate the following time-discretized corrected energy functional*

$$\begin{aligned} E_c^n = {} & \frac{1}{2}\left(|r^{n+1}|^2 + |2r^{n+1} - r^n|^2\right) + \frac{\epsilon^2}{4}\sum_{i=1}^{2}\left(\|\sqrt{1-\phi_0}\nabla\phi_i^{n+1}\|^2 + \|\sqrt{1-\phi_0}(2\nabla\phi_i^{n+1} - \nabla\phi_i^n\|^2)\|^2\right) \\ & + \frac{S}{2}\sum_{i=1}^{2}\|\phi_i^{n+1} - \phi_i^n\|^2 + \frac{We}{4}\left(\|\mathbf{u}^{n+1}\|^2 + \|2\mathbf{u}^{n+1} - \mathbf{u}^n\|^2\right) + \frac{1}{4}(|q^{n+1}|^2 + |2q^{n+1} - q^n|^2) \\ & + \frac{We\Delta t^2}{3}\|\nabla p^{n+1}\|^2 - \frac{1}{2}. \end{aligned} \tag{3.25}$$

Proof. By taking the L^2-inner product of Eq. (3.10) with $\Delta t \mu_i^{n+1}$, we get

$$\left(3\phi_i^{n+1} - 4\phi_i^n + \phi_i^{n-1}, \mu_i^{n+1}\right) + 2\Delta t \hat{q}^{n+1}\left(\nabla\cdot(\mathbf{u}^*\phi_i^*), \mu_i^{n+1}\right) = -\frac{2\Delta t}{Pe}\|\sqrt{1-\phi_0}\nabla\mu_i^{n+1}\|^2. \tag{3.26}$$

By taking the L^2-inner product of Eq. (3.11) with $3\phi_i^{n+1} - 4\phi_i^n + \phi_i^{n-1}$, we have

$$\begin{aligned} \left(\mu_i^{n+1}, 3\phi_i^{n+1} - 4\phi_i^n + \phi_i^{n-1}\right) = {} & \left(\hat{r}^{n+1}H_i^*, 3\phi_i^{n+1} - 4\phi_i^n + \phi_i^{n-1}\right) + \left(\hat{r}^{n+1}\beta(\boldsymbol{\phi}), 3\phi_i^{n+1} - 4\phi_i^n + \phi_i^{n-1}\right) \\ & + \frac{\epsilon^2}{2}\left(\|\sqrt{1-\phi_0}\nabla\phi_i^{n+1}\|^2 + \|\sqrt{1-\phi_0}(2\nabla\phi_i^{n+1} - \nabla\phi_i^n)\|^2\right) \\ & - \frac{\epsilon^2}{2}\left(\|\sqrt{1-\phi_0}\nabla\phi_i^n\|^2 + \|\sqrt{1-\phi_0}(2\nabla\phi_i^n - \nabla\phi_i^{n-1})\|^2\right) \\ & + \frac{\epsilon^2}{2}\|\sqrt{1-\phi_0}(\nabla\phi_i^{n+1} - 2\nabla\phi_i^n + \nabla\phi_i^{n-1})\|^2 + S\|\phi_i^{n+1} - \phi_i^n\|^2 \\ & - S\|\phi_i^n - \phi_i^{n-1}\|^2 + 2S\|\phi_i^{n+1} - 2\phi_i^n + \phi_i^{n-1}\|^2. \end{aligned} \tag{3.27}$$

By multiplying Eq. (3.15) with $2\hat{r}^{n+1}$, we have

$$\begin{aligned} & \left(|\hat{r}^{n+1}|^2 + |2\hat{r}^{n+1} - r^n|^2\right) - \left(|\hat{r}^n|^2 + |2\hat{r}^n - r^{n-1}|^2\right) + |\hat{r}^{n+1} - 2r^n + r^{n-1}|^2 \\ & = \left(\hat{r}^{n+1}\sum_{i=1}^{2}H_i^*, 3\phi_i^{n+1} - 4\phi_i^n + \phi_i^{n-1}\right). \end{aligned} \tag{3.28}$$

By combining Eqs. (3.26)–(3.28), we obtain

$$\begin{aligned}
&\frac{1}{2}\left(|\hat{r}^{n+1}|^2+|2\hat{r}^{n+1}-r^n|^2\right)-\frac{1}{2}\left(|\hat{r}^{n}|^2+|2\hat{r}^{n}-r^{n-1}|^2\right)\\
&+\frac{\epsilon^2}{4}\left(\|\sqrt{1-\phi_0}\nabla\phi_i^{n+1}\|^2+\|\sqrt{1-\phi_0}(2\nabla\phi_i^{n+1}-\nabla\phi_i^{n})\|^2\right)\\
&-\frac{\epsilon^2}{4}\left(\|\sqrt{1-\phi_0}\nabla\phi_i^{n}\|^2+\|\sqrt{1-\phi_0}(2\nabla\phi_i^{n}-\nabla\phi_i^{n-1})\|^2\right)+\frac{S}{2}\|\phi_i^{n+1}-\phi_i^{n}\|^2-\frac{S}{2}\|\phi_i^{n}-\phi_i^{n-1}\|^2\\
&+\Delta t\hat{q}^{n+1}\left(\nabla\cdot(\mathbf{u}^*\phi_i^*),\mu_i^{n+1}\right)=-\frac{\Delta t}{Pe}\|\sqrt{1-\phi_0}\nabla\mu_i^{n+1}\|^2-\frac{\epsilon^2}{4}\|\sqrt{1-\phi_0}(\nabla\phi_i^{n+1}-2\nabla\phi_i^{n}+\nabla\phi_i^{n-1})\|^2\\
&-S\|\phi_i^{n+1}-2\phi_i^{n}+\phi_i^{n-1}\|^2-\frac{1}{4}|\hat{r}^{n+1}-2r^n+r^{n-1}|^2-\left(\hat{r}^{n+1}H_i^*,3\phi_i^{n+1}-4\phi_i^{n}+\phi_i^{n-1}\right)\\
&+\left(\hat{r}^{n+1}\sum_{i=1}^{2}H_i^*,3\phi_i^{n+1}-4\phi_i^{n}+\phi_i^{n-1}\right).
\end{aligned}\tag{3.29}$$

By taking the L^2-inner product of Eq. (3.12) with $We\Delta t\tilde{\mathbf{u}}^{n+1}$, we get

$$\begin{aligned}
&\frac{We}{2}\underbrace{\left(3\tilde{\mathbf{u}}^{n+1}-4\mathbf{u}^{n}+\mathbf{u}^{n-1},\tilde{\mathbf{u}}^{n+1}\right)}_{\mathrm{I}}+We\Delta t\hat{q}^{n+1}\left(\mathbf{u}^*\cdot\nabla\mathbf{u}^*,\tilde{\mathbf{u}}^{n+1}\right)=-We\Delta t\left(\nabla p^n,\tilde{\mathbf{u}}^{n+1}\right)\\
&-\frac{We\Delta t}{Re}\|\nabla\tilde{\mathbf{u}}^{n+1}\|^2-\hat{q}^{n+1}\Delta t\left(\sum_{i=1}^{2}\phi_i^*\nabla\mu_i^*,\tilde{\mathbf{u}}^{n+1}\right)-\frac{We\Delta t}{\kappa}\|\sqrt{\phi_0}\tilde{\mathbf{u}}^{n+1}\|^2,
\end{aligned}\tag{3.30}$$

where the term I can be estimated as follows

$$\begin{aligned}
&\left(3\tilde{\mathbf{u}}^{n+1}-4\mathbf{u}^{n}+\mathbf{u}^{n-1},\tilde{\mathbf{u}}^{n+1}\right)\\
&=\left(3\tilde{\mathbf{u}}^{n+1}-4\mathbf{u}^{n}+\mathbf{u}^{n-1},\mathbf{u}^{n+1}\right)+\left(3\tilde{\mathbf{u}}^{n+1}-4\mathbf{u}^{n}+\mathbf{u}^{n-1},\tilde{\mathbf{u}}^{n+1}-\mathbf{u}^{n+1}\right)\\
&=\left(3\mathbf{u}^{n+1}-4\mathbf{u}^{n}+\mathbf{u}^{n-1},\mathbf{u}^{n+1}\right)+\left(3\tilde{\mathbf{u}}^{n+1},\tilde{\mathbf{u}}^{n+1}-\mathbf{u}^{n+1}\right)\\
&=\left(3\mathbf{u}^{n+1}-4\mathbf{u}^{n}+\mathbf{u}^{n-1},\mathbf{u}^{n+1}\right)+3\left(\tilde{\mathbf{u}}^{n+1}-\mathbf{u}^{n+1},\tilde{\mathbf{u}}^{n+1}+\mathbf{u}^{n+1}\right)\\
&=\frac{1}{2}\left(\|\mathbf{u}^{n+1}\|^2-\|\mathbf{u}^{n}\|^2+\|2\mathbf{u}^{n+1}-\mathbf{u}^{n}\|^2-\|2\mathbf{u}^{n}-\mathbf{u}^{n-1}\|^2+\|\mathbf{u}^{n+1}-2\mathbf{u}^{n}+\mathbf{u}^{n-1}\|^2\right)\\
&\quad+3\left(\|\tilde{\mathbf{u}}^{n+1}\|^2-\|\mathbf{u}^{n+1}\|^2\right).
\end{aligned}$$

From Eq. (3.13), we have

$$\frac{3\mathbf{u}^{n+1}}{2\Delta t}+\nabla p^{n+1}=\frac{3\tilde{\mathbf{u}}^{n+1}}{2\Delta t}+\nabla p^{n}.\tag{3.31}$$

By squaring the above equality and taking the integral, we have

$$\Delta t\left(\nabla p^n,\tilde{\mathbf{u}}^{n+1}\right)=\frac{3}{4}\|\mathbf{u}^{n+1}\|^2-\frac{3}{4}\|\tilde{\mathbf{u}}^{n+1}\|^2+\frac{\Delta t^2}{3}\left(\|\nabla p^{n+1}\|^2-\|\nabla p^{n}\|^2\right).\tag{3.32}$$

By combining Eqs. (3.30) and (3.32), we get

$$\begin{aligned}
&\frac{We}{2}\left(\|\mathbf{u}^{n+1}\|^2-\|\mathbf{u}^{n}\|^2+\|2\mathbf{u}^{n+1}-\mathbf{u}^{n}\|^2-\|2\mathbf{u}^{n}-\mathbf{u}^{n-1}\|^2+\|\mathbf{u}^{n+1}-2\mathbf{u}^{n}+\mathbf{u}^{n-1}\|^2\right)\\
&+\frac{3We}{2}\|\tilde{\mathbf{u}}^{n+1}\|^2-\frac{3We}{2}\|\mathbf{u}^{n+1}\|^2+2We\Delta t\hat{q}^{n+1}\left(\mathbf{u}^*\cdot\nabla\mathbf{u}^*,\tilde{\mathbf{u}}^{n+1}\right)+2\Delta t\hat{q}^{n+1}\left(\sum_{i=1}^{2}\phi_i^*\nabla\mu_i^*,\tilde{\mathbf{u}}^{n+1}\right)\\
&=-\frac{2We\Delta t}{Re}\|\nabla\tilde{\mathbf{u}}^{n+1}\|^2-\frac{2We\Delta t^2}{3}\left(\|\nabla p^{n+1}\|^2-\|\nabla p^{n}\|^2\right)-\frac{2We\Delta t}{\kappa}\|\sqrt{\phi_0}\tilde{\mathbf{u}}^{n+1}\|^2.
\end{aligned}\tag{3.33}$$

By taking the L^2-inner product of Eq. (3.31) with $2\Delta t\mathbf{u}^{n+1}$, we have

$$\frac{3}{2}\|\tilde{\mathbf{u}}^{n+1}\|^2-\frac{3}{2}\|\mathbf{u}^{n+1}\|^2=\frac{3}{2}\|\mathbf{u}^{n+1}-\tilde{\mathbf{u}}^{n+1}\|^2.\tag{3.34}$$

By multiplying Eq. (3.16) with $\hat{q}^{n+1}$, we have

$$\frac{1}{2}\left(|\hat{q}^{n+1}|^2-|q^n|^2+|2\hat{q}^{n+1}-q^n|^2-|2q^n-q^{n-1}|^2\right)+\frac{1}{2}|\hat{q}^{n+1}-2q^n+q^{n-1}|^2$$
$$=2We\Delta t\hat{q}^{n+1}\left(\mathbf{u}^*\cdot\nabla\mathbf{u}^*,\tilde{\mathbf{u}}^{n+1}\right)+2\Delta t\hat{q}^{n+1}\sum_{i=1}^{2}\left(\nabla\cdot(\mathbf{u}^*\phi_i^*),\mu_i^{n+1}\right)+2\Delta t\hat{q}^{n+1}\sum_{i=1}^{2}\left(\phi_i^*\nabla\mu_i^*,\tilde{\mathbf{u}}^{n+1}\right). \tag{3.35}$$

By combining Eq. (3.29) with $i=1,2$ and Eqs. (3.33)–(3.35), we have

$$\underbrace{\frac{1}{2}\left(|\hat{r}^{n+1}|^2+|2\hat{r}^{n+1}-r^n|^2\right)}_{\text{I}}-\frac{1}{2}\left(|r^n|^2+|2r^n-r^{n-1}|^2\right)+\frac{We\Delta t}{3}\left(\|\nabla p^{n+1}\|^2-\|\nabla p^n\|^2\right)$$
$$+\frac{\epsilon^2}{4}\sum_{i=1}^{2}\left(\|\sqrt{1-\phi_0}\nabla\phi_i^{n+1}\|^2+\|\sqrt{1-\phi_0}(2\nabla\phi_i^{n+1}-\nabla\phi_i^n)\|^2\right)$$
$$-\frac{\epsilon^2}{4}\sum_{i=1}^{2}\left(\|\sqrt{1-\phi_0}\nabla\phi_i^{n}\|^2+\|\sqrt{1-\phi_0}(2\nabla\phi_i^{n}-\nabla\phi_i^{n-1})\|^2\right)$$
$$+\sum_{i=1}^{2}\left(\frac{S}{2}\|\phi_i^{n+1}-\phi_i^n\|^2-\frac{S}{2}\|\phi_i^n-\phi_i^{n-1}\|^2\right)+\frac{We}{4}\left(\|\mathbf{u}^{n+1}\|^2+\|2\mathbf{u}^{n+1}-\mathbf{u}^n\|^2\right)$$
$$-\frac{We}{4}\left(\|\mathbf{u}^{n}\|^2+\|2\mathbf{u}^{n}-\mathbf{u}^{n-1}\|^2\right)+\underbrace{\frac{1}{4}\left(|\hat{q}^{n+1}|^2+|2\hat{q}^{n+1}-q^n|^2\right)}_{\text{II}}-\frac{1}{4}\left(|q^n|^2+|2q^n-q^{n-1}|^2\right)$$
$$=-\frac{\Delta t}{Pe}\left(\sum_{i=1}^{2}\|\sqrt{1-\phi_0}\nabla\mu_i^{n+1}\|^2\right)-\frac{\epsilon^2}{2}\sum_{i=1}^{2}\|\sqrt{1-\phi_0}(\nabla\phi_i^{n+1}-2\nabla\phi_i^n+\nabla\phi_i^{n-1})\|^2$$
$$-S\sum_{i=1}^{2}\|\phi_i^{n+1}-2\phi_i^n+\phi_i^{n-1}\|^2-\frac{1}{2}|\hat{r}^{n+1}-2r^n+r^{n-1}|^2-\frac{We\Delta t}{Re}\|\nabla\tilde{\mathbf{u}}^{n+1}\|^2-\frac{We\Delta t}{\kappa}\|\sqrt{\phi_0}\tilde{\mathbf{u}}^{n+1}\|^2$$
$$-\frac{1}{4}|\hat{q}^{n+1}-2q^n+q^{n-1}|^2-\frac{3We}{4}\|\mathbf{u}^{n+1}-\tilde{\mathbf{u}}^{n+1}\|^2-\frac{We}{4}\|\mathbf{u}^{n+1}-2\mathbf{u}^n+\mathbf{u}^{n-1}\|^2. \tag{3.36}$$

Here, we notice that the term I and term II contain variables $\hat{r}^{n+1}$ and $\hat{q}^{n+1}$ without correction, thus the above inequality the proposed scheme satisfies the time-discretized energy dissipation law with respect to the following modified energy

$$E_m^n=\frac{1}{2}\left(|\hat{r}^{n+1}|^2+|2\hat{r}^{n+1}-r^n|^2\right)+\frac{\epsilon^2}{4}\sum_{i=1}^{2}\left(\|\sqrt{1-\phi_0}\nabla\phi_i^{n+1}\|^2+\|\sqrt{1-\phi_0}(2\nabla\phi_i^{n+1}-\nabla\phi_i^n\|^2)\|^2\right)$$
$$+\frac{S}{2}\sum_{i=1}^{2}\|\phi_i^{n+1}-\phi_i^n\|^2+\frac{We}{4}\left(\|\mathbf{u}^{n+1}\|^2+\|2\mathbf{u}^{n+1}-\mathbf{u}^n\|^2\right)+\frac{1}{4}(|\hat{q}^{n+1}|^2+|2\hat{q}^{n+1}-q^n|^2)$$
$$+\frac{We\Delta t^2}{3}\|\nabla p^{n+1}\|^2-\frac{1}{2}. \tag{3.37}$$

By combining Eq. (3.36), Eq. (3.18) and $\frac{1}{2}$ Eq. (3.22), we derive

$$\frac{1}{2}\left(|r^{n+1}|^2+|2r^{n+1}-r^n|^2\right)-\frac{1}{2}\left(|r^n|^2+|2r^n-r^{n-1}|^2\right)+\frac{We\Delta t}{3}\left(\|\nabla p^{n+1}\|^2-\|\nabla p^n\|^2\right)$$
$$+\frac{\epsilon^2}{4}\sum_{i=1}^{2}\left(\|\sqrt{1-\phi_0}\nabla\phi_i^{n+1}\|^2+\|\sqrt{1-\phi_0}(2\nabla\phi_i^{n+1}-\nabla\phi_i^n)\|^2\right)$$
$$-\frac{\epsilon^2}{4}\sum_{i=1}^{2}\left(\|\sqrt{1-\phi_0}\nabla\phi_i^{n}\|^2+\|\sqrt{1-\phi_0}(2\nabla\phi_i^{n}-\nabla\phi_i^{n-1})\|^2\right)$$
$$+\sum_{i=1}^{2}\left(\frac{S}{2}\|\phi_i^{n+1}-\phi_i^n\|^2-\frac{S}{2}\|\phi_i^n-\phi_i^{n-1}\|^2\right)+\frac{We}{4}\left(\|\mathbf{u}^{n+1}\|^2+\|2\mathbf{u}^{n+1}-\mathbf{u}^n\|^2\right)$$
$$-\frac{We}{4}\left(\|\mathbf{u}^{n}\|^2+\|2\mathbf{u}^{n}-\mathbf{u}^{n-1}\|^2\right)+\frac{1}{4}\left(|q^{n+1}|^2+|2q^{n+1}-q^n|^2\right)-\frac{1}{4}\left(|q^n|^2+|2q^n-q^{n-1}|^2\right)$$

$$= \underbrace{\Delta t\left(\eta_1 - \frac{1}{Pe}\right)\left(\sum_{i=1}^{2}\|\sqrt{1-\phi_0}\nabla\mu_i^{n+1}\|^2\right)}_{\text{I}} - \frac{\epsilon^2}{2}\sum_{i=1}^{2}\|\sqrt{1-\phi_0}(\nabla\phi_i^{n+1} - 2\nabla\phi_i^n + \nabla\phi_i^{n-1})\|^2$$

$$-S\sum_{i=1}^{2}\|\phi_i^{n+1} - 2\phi_i^n + \phi_i^{n-1}\|^2 - \frac{1}{2}|\hat{r}^{n+1} - 2r^n + r^{n-1}|^2 + \underbrace{\Delta t\left(\frac{\eta_2}{2} - \frac{We}{Re}\right)\|\nabla\tilde{\mathbf{u}}^{n+1}\|^2}_{\text{II}}$$

$$+\underbrace{\Delta t\left(\frac{\eta_2}{2} - \frac{We}{\kappa}\right)\|\sqrt{\phi_0}\tilde{\mathbf{u}}^{n+1}\|^2}_{\text{III}} - \frac{1}{4}|\hat{q}^{n+1} - 2q^n + q^{n-1}|^2 - \frac{3We}{4}\|\mathbf{u}^{n+1} - \tilde{\mathbf{u}}^{n+1}\|^2$$

$$-\frac{We}{4}\|\mathbf{u}^{n+1} - 2\mathbf{u}^n + \mathbf{u}^{n-1}\|^2. \tag{3.38}$$

Because of the choices of η_1 and η_2, terms I, II, III are non-positive. Therefore, the above inequality completes the proof. □

Remark 3.2. In this section, the energy dissipation property has been analytically estimated with appropriate boundary conditions. In the next section, various numerical simulations will be performed to examine the performance of our proposed method. It is worth noting that the cases with inlet and outlet, lid-driven velocity, and buoyancy-driven force do not follow the present energy dissipation law in general because the boundary effects cannot be easily eliminated. We will conduct these simulations to confirm that our model and method still work well in various settings. In our upcoming works, the similar idea in [39] will be considered to construct energy-stable scheme with inlet and outlet.

3.3. Totally decoupled numerical implementation

Although Eqs. (3.10)–(3.16) are linear, the local variables: ϕ_i^{n+1} and $\tilde{\mathbf{u}}^{n+1}$ and non-local variables: $\hat{r}^{n+1}$ and $\hat{q}^{n+1}$ are still weakly coupled. To achieve more efficient and totally decoupled computation, we herein introduce the implementation of splitting algorithms. We define $\phi_{i,1}^{n+1}$, $\phi_{i,2}^{n+1}$, $\mu_{i,1}^{n+1}$, $\mu_{i,2}^{n+1}$, $\tilde{\mathbf{u}}_1^{n+1}$, $\tilde{\mathbf{u}}_2^{n+1}$, $\hat{r}_1^{n+1}$, and $\hat{r}_2^{n+1}$ as new intermediate variables. Since $\hat{q}^{n+1}$ is a time-dependent variable, we let

$$\phi_i^{n+1} = \phi_{i,1}^{n+1} + \hat{q}^{n+1}\phi_{i,2}^{n+1}, \quad \mu_i^{n+1} = \mu_{i,1}^{n+1} + \hat{q}^{n+1}\mu_{i,2}^{n+1}, \tag{3.39}$$

$$\hat{r}^{n+1} = \hat{r}_1^{n+1} + \hat{q}^{n+1}\hat{r}_2^{n+1}, \quad \tilde{\mathbf{u}}^{n+1} = \tilde{\mathbf{u}}_1^{n+1} + \hat{q}^{n+1}\tilde{\mathbf{u}}_2^{n+1}. \tag{3.40}$$

Equations (3.10) and (3.11) are recast to be

$$\frac{3\phi_{i,1}^{n+1} + 3\hat{q}^{n+1}\phi_{i,2}^{n+1} - 4\phi_i^n + \phi_i^{n-1}}{2\Delta t} + \hat{q}^{n+1}\nabla\cdot(\mathbf{u}^*\phi_i^*) = \frac{1}{Pe}\nabla\cdot((1-\phi_0)\nabla(\mu_{i,1}^{n+1} + \hat{q}^{n+1}\mu_{i,2}^{n+1})), \tag{3.41}$$

$$\mu_{i,1}^{n+1} + \hat{q}^{n+1}\mu_{i,2}^{n+1} = (\hat{r}_1^{n+1} + \hat{q}^{n+1}\hat{r}_2^{n+1})(H_i^* + \beta(\boldsymbol{\phi}^*)) - \epsilon^2\nabla\cdot((1-\phi_0)\nabla(\phi_{i,1}^{n+1} + \hat{q}^{n+1}\phi_{i,2}^{n+1}))$$
$$+S(\phi_{i,1}^{n+1} + \hat{q}^{n+1}\phi_{i,2}^{n+1} - \phi_i^*). \tag{3.42}$$

The above equality can be split into

$$\frac{3\phi_{i,1}^{n+1} - 4\phi_i^n + \phi_i^{n-1}}{2\Delta t} = \frac{1}{Pe}\nabla\cdot((1-\phi_0)\nabla\mu_{i,1}^{n+1}), \tag{3.43}$$

$$\mu_{i,1}^{n+1} = \hat{r}^{n+1}(H_i^* + \beta(\boldsymbol{\phi}^*)) - \epsilon^2\nabla\cdot((1-\phi_0)\nabla\phi_{i,1}^{n+1}) + S(\phi_{i,1}^{n+1} - \phi_i^*), \tag{3.44}$$

and

$$\frac{3\phi_{i,2}^{n+1}}{2\Delta t} + \nabla\cdot(\mathbf{u}^*\phi_i^*) = \frac{1}{Pe}\nabla\cdot((1-\phi_0)\nabla\mu_{i,2}^{n+1}), \tag{3.45}$$

$$\mu_{i,2}^{n+1} = \hat{r}^{n+1}(H_i^* + \beta(\boldsymbol{\phi}^*)) - \epsilon^2\nabla\cdot((1-\phi_0)\nabla\phi_{i,2}^{n+1}) + S\phi_{i,2}^{n+1}. \tag{3.46}$$

By defining extra variables: $\phi_{i,11}^{n+1}$, $\phi_{i,12}^{n+1}$, $\phi_{i,21}^{n+1}$, $\phi_{i,22}^{n+1}$ and $\mu_{i,11}^{n+1}$, $\mu_{i,12}^{n+1}$, $\mu_{i,21}^{n+1}$, $\mu_{i,22}^{n+1}$. We let

$$\phi_{i,1}^{n+1} = \phi_{i,11}^{n+1} + \hat{r}_1^{n+1}\phi_{i,12}^{n+1}, \quad \mu_{i,1}^{n+1} = \mu_{i,11}^{n+1} + \hat{r}_1^{n+1}\mu_{i,12}^{n+1}, \tag{3.47}$$

$$\phi_{i,2}^{n+1} = \phi_{i,21}^{n+1} + \hat{r}_2^{n+1}\phi_{i,22}^{n+1}, \quad \mu_{i,2}^{n+1} = \mu_{i,21}^{n+1} + \hat{r}_2^{n+1}\mu_{i,22}^{n+1}. \tag{3.48}$$

Then we can split Eqs. (3.43) and (3.44) into

$$\frac{3\phi_{i,11}^{n+1}-4\phi_i^n+\phi_i^{n-1}}{2\Delta t}=\frac{1}{Pe}\nabla\cdot((1-\phi_0)\nabla\mu_{i,11}^{n+1}), \tag{3.49}$$

$$\mu_{i,11}^{n+1}=-\epsilon^2\nabla\cdot((1-\phi_0)\nabla\phi_{i,11}^{n+1})+S(\phi_{i,11}^{n+1}-\phi_i^*), \tag{3.50}$$

and

$$\frac{3\phi_{i,12}^{n+1}}{2\Delta t}=\frac{1}{Pe}\nabla\cdot((1-\phi_0)\nabla\mu_{i,12}^{n+1}), \tag{3.51}$$

$$\mu_{i,12}^{n+1}=H_i^*+\beta(\boldsymbol{\phi}^*)-\epsilon^2\nabla\cdot((1-\phi_0)\nabla\phi_{i,12}^{n+1})+S\phi_{i,12}^{n+1}. \tag{3.52}$$

Equations (3.45) and (3.46) are split into

$$\frac{3\phi_{i,21}^{n+1}}{2\Delta t}+\nabla\cdot(\mathbf{u}*\phi_i^*)=\frac{1}{Pe}\nabla\cdot((1-\phi_0)\nabla\mu_{i,21}^{n+1}), \tag{3.53}$$

$$\mu_{i,21}^{n+1}=-\epsilon^2\nabla\cdot((1-\phi_0)\nabla\phi_{i,21}^{n+1})+S\phi_{i,21}^{n+1}, \tag{3.54}$$

and

$$\frac{3\phi_{i,22}^{n+1}}{2\Delta t}=\frac{1}{Pe}\nabla\cdot((1-\phi_0)\nabla\mu_{i,22}^{n+1}), \tag{3.55}$$

$$\mu_{i,22}^{n+1}=H_i^*+\beta(\boldsymbol{\phi}^*)-\epsilon^2\nabla\cdot((1-\phi_0)\nabla\phi_{i,22}^{n+1})+S\phi_{i,22}^{n+1}. \tag{3.56}$$

From Eqs. (3.49)–(3.56), we obtain the solutions of $\phi_{i,11}^{n+1}$, $\phi_{i,12}^{n+1}$, $\phi_{i,21}^{n+1}$, $\phi_{i,22}^{n+1}$ and $\mu_{i,11}^{n+1}$, $\mu_{i,12}^{n+1}$, $\mu_{i,21}^{n+1}$, $\mu_{i,22}^{n+1}$ via solving several linear and totally decoupled elliptic type equations. Therefore, the calculations are simple to implement. By recasting Eq. (3.15), we have

$$3\hat{r}_1^{n+1}+3\hat{q}^{n+1}\hat{r}_2^{n+1}-4r^n+r^{n-1}=\frac{1}{2}\int_\Omega\sum_{i=1}^{2}H_i^*(3\phi_{i,1}^{n+1}+3\hat{q}^{n+1}\phi_{i,2}^{n+1}-4\phi_i^n+\phi_i^{n-1})\,d\mathbf{x}. \tag{3.57}$$

By using the definitions of $\phi_{i,1}^{n+1}$ and $\phi_{i,2}^{n+1}$, we split the above equality into

$$3\hat{r}_1^{n+1}-4r^n+r^{n-1}=\frac{1}{2}\int_\Omega\sum_{i=1}^{2}H_i^*(3\phi_{i,11}^{n+1}+3\hat{r}_1^{n+1}\phi_{i,12}^{n+1}-4\phi_i^n+\phi_i^{n-1})\,d\mathbf{x}, \tag{3.58}$$

and

$$3\hat{r}_2^{n+1}=\frac{1}{2}\int_\Omega\sum_{i=1}^{2}H_i^*(3\phi_{i,21}^{n+1}+3\hat{r}_2^{n+1}\phi_{i,22}^{n+1})\,d\mathbf{x}. \tag{3.59}$$

From Eqs. (3.58) and (3.59), we obtain the solutions of $\hat{r}_1^{n+1}$ and $\hat{r}_2^{n+1}$ as follows

$$\left(3-\frac{3}{2}\int_\Omega\sum_{i=1}^{2}H_i^*\phi_{i,12}^{n+1}\,d\mathbf{x}\right)\hat{r}_1^{n+1}=4r^n-r^{n-1}+\frac{1}{2}\int_\Omega\sum_{i=1}^{2}H_i^*(3\phi_{i,11}^{n+1}-4\phi_i^n+\phi_i^{n-1})\,d\mathbf{x}. \tag{3.60}$$

$$\left(3-\frac{3}{2}\int_\Omega\sum_{i=1}^{2}H_i^*\phi_{i,22}^{n+1}\,d\mathbf{x}\right)\hat{r}_2^{n+1}=\frac{3}{2}\int_\Omega\sum_{i=1}^{2}H_i^*\phi_{i,21}^{n+1}\,d\mathbf{x}. \tag{3.61}$$

By recasting Eq. (3.12), we get

$$\begin{aligned}\frac{3\tilde{\mathbf{u}}_1^{n+1}+3\hat{q}^{n+1}\tilde{\mathbf{U}}_2^{n+1}-4\mathbf{u}^n+\mathbf{u}^{n-1}}{2\Delta t}+\hat{q}^{n+1}\mathbf{u}^*\cdot\nabla\mathbf{u}^*=&-\nabla p^n+\frac{1}{Re}\left(\Delta\tilde{\mathbf{u}}_1^{n+1}+\hat{q}^{n+1}\Delta\tilde{\mathbf{u}}_2^{n+1}\right)\\&-\frac{\hat{q}^{n+1}}{We}\sum_{i=1}^{2}\phi_i^*\nabla\mu_i^*-\frac{\phi_0}{\kappa}(\tilde{\mathbf{u}}_1^{n+1}+\hat{q}^{n+1}\tilde{\mathbf{u}}_2^{n+1}).\end{aligned} \tag{3.62}$$

We split the above equality into

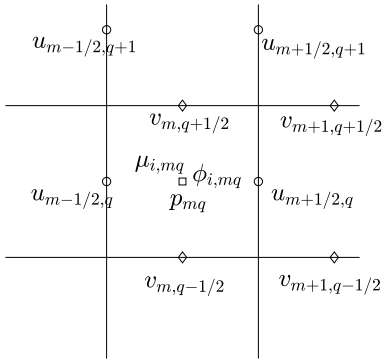

Fig. 2. Schematic illustration of staggered marker-and-cell (MAC) mesh grids.

$$\frac{3\tilde{\mathbf{u}}^{n+1}-4\mathbf{u}^{n}+\mathbf{u}^{n-1}}{2\Delta t}=-\nabla p^{n}+\frac{1}{Re}\Delta\tilde{\mathbf{u}}_1^{n+1}-\frac{\phi_0}{\kappa}\tilde{\mathbf{u}}_1^{n+1}, \tag{3.63}$$

$$\frac{3\tilde{\mathbf{u}}_2^{n+1}}{2\Delta t}+\mathbf{u}^{*}\cdot\nabla\mathbf{u}^{*}=\frac{1}{Re}\Delta\tilde{\mathbf{u}}_2^{n+1}-\frac{1}{We}\sum_{i=1}^{2}\phi_i^{*}\nabla\mu_i^{*}-\frac{\phi_0}{\kappa}\tilde{\mathbf{u}}_2^{n+1}. \tag{3.64}$$

From the above equations, we update $\tilde{\mathbf{u}}_1^{n+1}$ and $\tilde{\mathbf{u}}_2^{n+1}$. With these computed values from previous equations, Eq. (3.16) is recast to be

$$\begin{aligned}3\hat{q}^{n+1}-4q^{n}+q^{n-1}=2\Delta t\int_{\Omega}\sum_{i=1}^{2}\Big[\nabla\cdot(\mathbf{u}^{*}\phi_i^{*})(\mu_{i,1}^{n+1}+\hat{q}^{n+1}\mu_{i,2}^{n+1})\Big]+\sum_{i=1}^{2}\phi_i^{*}\nabla\mu_i^{*}(\tilde{\mathbf{u}}_i^{n+1}+\hat{q}^{n+1}\tilde{\mathbf{u}}_2^{n+1})\\ +We\mathbf{u}^{*}\cdot\nabla\mathbf{u}^{*}\cdot(\tilde{\mathbf{u}}^{n+1}+\hat{q}^{n+1}\tilde{\mathbf{u}}_2^{n+1})\,d\mathbf{x}.\end{aligned} \tag{3.65}$$

Then, we obtain $\hat{q}^{n+1}$ from the following equality

$$\begin{aligned}&\left(3-2\Delta t\int_{\Omega}\sum_{i=1}^{2}\Big[\nabla\cdot(\mathbf{u}^{*}\phi_i^{*})\mu_{i,2}^{n+1}\Big]+\sum_{i=1}^{2}\phi_i^{*}\nabla\mu_i^{*}\tilde{\mathbf{u}}_2^{n+1}+We\mathbf{u}^{*}\cdot\nabla\mathbf{u}^{*}\cdot\tilde{\mathbf{u}}_2^{n+1}\,d\mathbf{x}\right)\hat{q}^{n+1}\\ &=4q^{n}-q^{n-1}+2\Delta t\int_{\Omega}\sum_{i=1}^{2}\Big[\nabla\cdot(\mathbf{u}^{*}\phi_i^{*})\mu_{i,1}^{n+1}\Big]+\sum_{i=1}^{2}\phi_i^{*}\nabla\mu_i^{*}\tilde{\mathbf{u}}_1^{n+1}+We\mathbf{u}^{*}\cdot\nabla\mathbf{u}^{*}\cdot\tilde{\mathbf{u}}_1^{n+1}\,d\mathbf{x}.\end{aligned} \tag{3.66}$$

With computed $\hat{q}^{n+1}$, we can successively update other variables (i.e., ϕ_i^{n+1}, μ_i^{n+1}, $\tilde{\mathbf{u}}^{n+1}$, and $\hat{r}^{n+1}$) through back substitution. By applying the divergence-free condition in Eq. (3.14) into Eq. (3.13), the pressure is obtained by solving a Poisson equation. Finally, we explicitly update $\mathbf{u}^{n+1}$ from Eq. (3.13).

3.4. Fully discrete version

In this subsection, we briefly describe the finite difference method (FDM) for the spatial discretization. We only consider a 2D domain $\Omega=(0,L_1)\times(0,L_2)$ since the extension to 3D is straightforward. The uniform spatial step (mesh size) is defined as $h=L_1/N_1=L_2/N_2$, where N_1 and N_2 are even positive integers along x- and y-directions. In this work, the staggered marker-and-cell (MAC) mesh [40] is considered. As shown in Fig. 2, the velocities (u,v) are stored at cell edges, the phase-field function ϕ_i, the chemical potential μ_i, and the pressure p are stored at cell centers. The grid points locate at $x_m=(m-0.5)h$ and $y_q=(q-0.5)h$, where $m=1,2,\ldots,N_1$ and $q=1,2,\ldots,N_2$. Let c be an arbitrary variable locating at cell center, we define c_{mq}^{n} as the approximation of $c(x_m,y_q,n\Delta t)$, $u_{m+\frac{1}{2},q}^{n}$ and $v_{m,q+\frac{1}{2}}^{n}$ as the approximations of $u(x_{m+\frac{1}{2}},y_q,n\Delta t)$ and $v(x_m,y_{q+\frac{1}{2}},n\Delta t)$, respectively.

Some discrete operations are defined to be

$$\nabla_d c_{mq}=\Big(D_x c_{m+\frac{1}{2},q},D_y c_{m,q+\frac{1}{2}}\Big),\ D_x c_{m+\frac{1}{2},q}=\frac{c_{m+1,q}-c_{mq}}{h},\ D_y c_{m,q+\frac{1}{2}}=\frac{c_{m,q+1}-c_{mq}}{h},$$

$$\Delta_d c_{mq}=\frac{c_{m+1,q}+c_{m-1,q}+c_{m,q+1}+c_{m,q-1}-4c_{mq}}{h},$$

$$(c,\vartheta)_d=h^2\sum_{m=1}^{N_1}\sum_{q=1}^{N_2}c_{mq}\vartheta_{mq},$$

$$\nabla_d\cdot(c\mathbf{u})_{mq}=\frac{u_{m+\frac12,q}(c_{m+1,q}+c_{mq})-u_{m-\frac12,q}(c_{mq}+c_{m-1,q})}{2h}+\frac{v_{m,q+\frac12}(c_{m,q+1}+c_{mq})-v_{m,q-\frac12}(c_{mq}+c_{m,q-1})}{2h},$$

$$|\nabla_d c_{mq}|^2=\frac{(c_{m+1,q}-c_{m-1,q})^2}{4h^2}+\frac{(c_{m,q+1}-c_{m,q-1})^2}{4h^2},$$

$$\nabla_d\cdot(\vartheta\nabla_d c)_{mq}=\frac{\vartheta_{m+\frac12,q}c_{m+1,q}+\vartheta_{m-\frac12,q}c_{m-1,q}+\vartheta_{m,q+\frac12}c_{m,q+1}+\vartheta_{m,q-\frac12}c_{m,q-1}}{h^2}-\left(\frac{\vartheta_{m+\frac12,q}+\vartheta_{m-\frac12,q}+\vartheta_{m,q+\frac12}+\vartheta_{m,q-\frac12}}{h^2}\right)c_{mq},$$

where ϑ locates at cell center, $\vartheta_{m+\frac12,q}=0.5(\vartheta_{m+1,q}+\vartheta_{mq})$ and other quantities are similarly defined. For the discrete functions like $f_{m+\frac12,q}$ and $g_{m+\frac12,q}$, we define the discrete inner product as

$$(f,g)_e=\frac{h^2}{2}\sum_{m=1}^{N_1}\sum_{q=1}^{N_2}\left(f_{m+\frac12,q}g_{m+\frac12,q}+f_{m-\frac12,q}g_{m-\frac12,q}\right).$$

For the discrete functions like $f_{m,q+\frac12}$ and $g_{m,q+\frac12}$, we define the discrete inner product as

$$(f,g)_h=\frac{h^2}{2}\sum_{m=1}^{N_1}\sum_{q=1}^{N_2}\left(f_{m,q+\frac12}g_{m,q+\frac12}+f_{m,q-\frac12}g_{m,q-\frac12}\right).$$

For the advection term $\mathbf{u}\cdot\nabla\mathbf{u}$, the central difference discretization [31] can be adopted to satisfy the fully discrete energy estimation. Here, $(\mathbf{u}\cdot\nabla\mathbf{u})_x$ and $(\mathbf{u}\cdot\nabla\mathbf{u})_y$ represent the spatial discretizations of advection term along x- and y-directions. The fully discrete FDM of Eqs. (3.10)–(3.16) reads as

$$\frac{3\phi_{i,mq}^{n+1}-4\phi_{i,mq}^{n}+\phi_{i,mq}^{n-1}}{2\Delta t}+\hat{q}^{n+1}\nabla_d\cdot(\mathbf{u}^*\phi_i^*)_{mq}=\frac{1}{Pe}\nabla_d\cdot((1-\phi_0)\nabla_d\mu_i^{n+1})_{mq},\tag{3.67}$$

$$\mu_{i,mq}^{n+1}=\hat{r}^{n+1}\left(H_{i,mq}^*+\beta(\boldsymbol{\phi}^*)_{mq}\right)-\epsilon^2\nabla_d\cdot\left((1-\phi_0)\nabla_d\phi_i^{n+1}\right)_{mq}+S(\phi_{i,mq}^{n+1}-\phi_{i,mq}^*),\quad i=1,2,\tag{3.68}$$

$$\frac{3\tilde{u}_{m+\frac12,q}^{n+1}-4u_{m+\frac12,q}^{n}+u_{m+\frac12,q}^{n-1}}{2\Delta t}+\hat{q}^{n+1}(\mathbf{u}^*\cdot\nabla\mathbf{u}^*)_x=-D_x p_{m+\frac12,q}^{n}-\frac{\hat{q}^{n+1}}{We}\sum_{i=1}^{2}\frac12\left(\phi_{m+1,q}^*+\phi_{mq}^*\right)D_x\mu_{i,m+\frac12,q}^*$$
$$+\frac{1}{Re}\left(\frac{\tilde{u}_{m+\frac32,q}^{n+1}+\tilde{u}_{m-\frac12,q}^{n+1}+\tilde{u}_{m+\frac12,q+1}^{n+1}+\tilde{u}_{m+\frac12,q-1}^{n+1}-4\tilde{u}_{m+\frac12,q}^{n+1}}{h^2}\right)-\frac{0.5(\phi_{0,m+1,q}+\phi_{0,mq})}{\kappa}\tilde{u}_{m+\frac12,q}^{n+1},\tag{3.69}$$

$$\frac{3\tilde{v}_{m,q+\frac12}^{n+1}-4v_{m,q+\frac12}^{n}+v_{m,q+\frac12}^{n-1}}{2\Delta t}+\hat{q}^{n+1}(\mathbf{u}^*\cdot\nabla\mathbf{u}^*)_y=-D_y p_{m,q+\frac12}^{n}-\frac{\hat{q}^{n+1}}{We}\sum_{i=1}^{2}\frac12\left(\phi_{m,q+1}^*+\phi_{mq}^*\right)D_y\mu_{i,m,q+\frac12}^*$$
$$+\frac{1}{Re}\left(\frac{\tilde{v}_{m,q+\frac32}^{n+1}+\tilde{v}_{m,q-\frac12}^{n+1}+\tilde{v}_{m+1,q+\frac12}^{n+1}+\tilde{v}_{m-1,q+\frac12}^{n+1}-4\tilde{v}_{m,q+\frac12}^{n+1}}{h^2}\right)-\frac{0.5(\phi_{0,m,q+1}+\phi_{0,mq})}{\kappa}\tilde{v}_{m,q+\frac12}^{n+1},\tag{3.70}$$

$$\frac{3u_{m+\frac12,q}^{n+1}-3\tilde{u}_{m+\frac12,q}^{n+1}}{2\Delta t}=-\left(D_x p_{m+\frac12,q}^{n+1}-D_x p_{m+\frac12,q}^{n}\right),\tag{3.71}$$

$$\frac{3v_{m,q+\frac12}^{n+1}-3\tilde{v}_{m,q+\frac12}^{n+1}}{2\Delta t}=-\left(D_y p_{m,q+\frac12}^{n+1}-D_y p_{m,q+\frac12}^{n}\right),\tag{3.72}$$

$$\frac{u_{m+\frac12,q}^{n+1}-u_{m-\frac12,q}^{n+1}}{h}+\frac{v_{m,q+\frac12}^{n+1}-v_{m,q-\frac12}^{n+1}}{h}=0,\tag{3.73}$$

$$3\hat{r}^{n+1}-4r^{n}+r^{n-1}=\frac12\sum_{i=1}^{2}\left(H_i^*,3\phi_i^{n+1}-4\phi_i^{n}+\phi_i^{n-1}\right)_d,\tag{3.74}$$

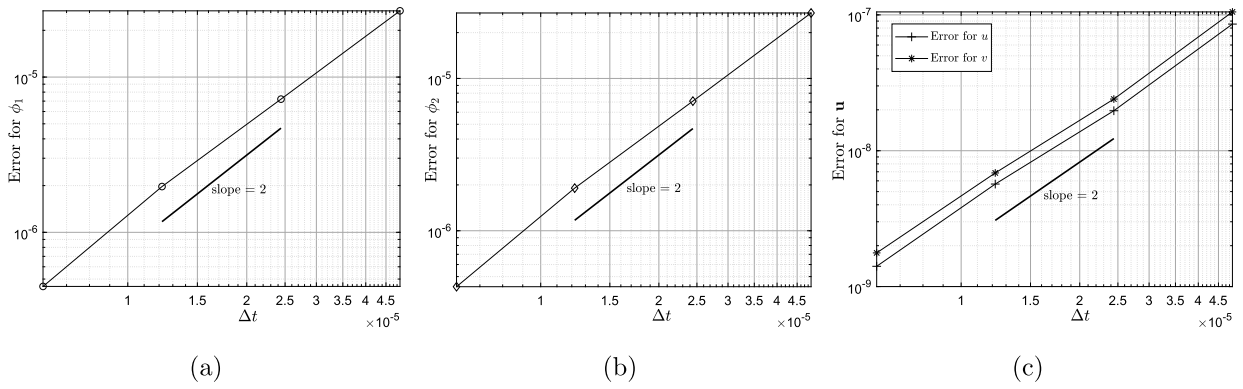

Fig. 3. Discrete L^2-errors with respect to ϕ_1 (a), ϕ_2 (b), and velocity field (c). In each figure, the black solid line is the reference with slope $= 2$.

$$\frac{3\hat{q}^{n+1} - 4q^n + q^{n-1}}{2\Delta t} = \sum_{i=1}^{2}\Bigg[(\nabla_d \cdot (\mathbf{u}^*\phi_i^*), \mu_i^{n+1})_d + \left(\frac{1}{2}(\phi^*_{i,m+1,q} + \phi^*_{i,mq})D_x\mu_i^*, \tilde{u}^{n+1}\right)_e$$
$$+ \left(\frac{1}{2}(\phi^*_{i,m,q+1} + \phi^*_{i,mq})D_y\mu_i^*, \tilde{v}^{n+1}\right)_h + We\left(\mathbf{u}^* \cdot \nabla\mathbf{u}^*)_x, \tilde{u}^{n+1}\right)_e + We\left(\mathbf{u}^* \cdot \nabla\mathbf{u}^*)_y, \tilde{v}^{n+1}\right)_h\Bigg]. \tag{3.75}$$

The fully discrete FDM is used to solve each subproblems in the previous subsection.

4. Computational tests

We herein perform various computational experiments to validate the accuracy, the energy law, and the capability of our proposed model and numerical scheme. In the following simulations, we set $\kappa = 10^{-8}$, $\eta_1 = 0.985/Pe$, and $\eta_2 = 1.985\min\{We/Re,\ We/\kappa\}$. The complex domains are embedded into a rectangular domain and a cubic domain in 2D and 3D spaces, respectively. The spatial discretization is performed with finite difference method, see [41,42] for some details. The dimensionless numbers are defined as: Reynolds number $Re = \rho_c U_c L_c/\eta_c$, Weber number $We = \rho_c U_c^2 L_c/\sigma$, Peclet number $Pe = U_c L_c/(M\mu_c)$. Here, M is the mobility, μ_c is the characteristic chemical potential. We can set $\rho_c = \rho_1$ and $\eta_c = \eta^1$ as the characteristic density and characteristic viscosity, ρ_1 and η^1 are density and viscosity of fluid 1. L_c is the characteristic length. For a droplet on the solid substrate, L_c is set to be the diameter of droplet or cylinder. For the simulation with initial velocity or exterior velocity (e.g. the inflow or the lid-driven flow), we define the characteristic velocity U_c as the initial velocity, inlet velocity, or lid-driven velocity. Otherwise, the characteristic velocity is defined as $U_c = L_c/T_c$, where T_c is the characteristic time.

4.1. Accuracy and energy stability

We first validate the accuracy of the proposed second-order time-marching scheme. For a fluid flow-coupled two-material system in an irregular domain, the exact solutions are hard to define in general. Therefore, we consider the numerical reference solutions which are obtained by using finer time step, i.e., $\Delta t^f = 0.05h^2$, where $h = 1/128$ (i.e., 128×128 grids) is the mesh size in a 2D unit computational domain. The initial conditions of ϕ_i $(i = 0, 1, 2)$ are defined as

$$\phi_0(x, y, 0) = 0.5 + 0.5\tanh\left(\frac{0.5 - \sqrt{(x-0.5)^2 + (y+0.25)^2}}{\sqrt{2}\epsilon}\right), \tag{4.1}$$

$$\phi_1(x, y, 0) = (1 - \phi_0(x, y, 0))\left(\frac{0.25 - \sqrt{(x-0.5)^2 + (y-0.2)^2}}{\sqrt{2}\epsilon}\right), \tag{4.2}$$

$$\phi_2(x, y, 0) = 1 - \phi_0(x, y, 0) - \phi_1(x, y, 0). \tag{4.3}$$

The initial velocities and pressure are zero. On the left and right boundaries, all variables are periodic. On the top and bottom boundaries, the zero Neumann boundary condition is considered for ϕ_i and pressure, the no-slip boundary condition is used for velocities. The parameters are set to be $Pe = Re = We = 1$, $\theta = 120°$, $\epsilon = 0.0038$ (almost 4 grids in diffuse interface). To calculate discrete L^2-errors, we compare the reference solutions with the numerical solutions computed by a set of increasingly coarser time steps: $\Delta t = 2\Delta t^f,\ 4\Delta t^f,\ 8\Delta t^f, 16\Delta t^f$. The computations are performed until $t = 256\Delta t^f$. Figs. 3(a), (b), and (c) plot the errors with respect to ϕ_1, ϕ_2, and velocities, respectively. In each figure, the black solid line has is the reference with slope $= 2$. The numerical results indicate that the proposed scheme is second-order accurate in time.

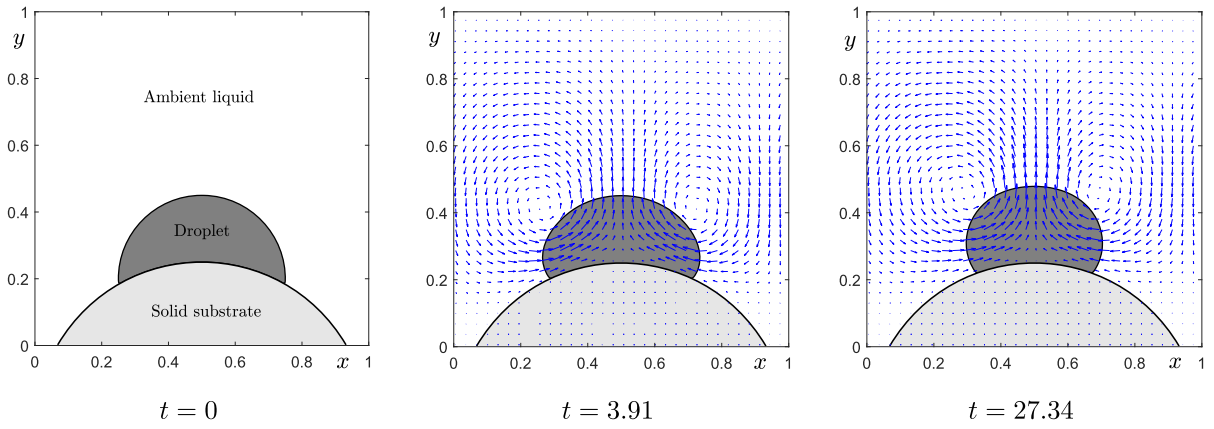

Fig. 4. Snapshots of droplet on an irregular solid substrate. The computational moments are shown under each figure. The blue arrows represent the velocity field. (For interpretation of the colors in the figure(s), the reader is referred to the web version of this article.)

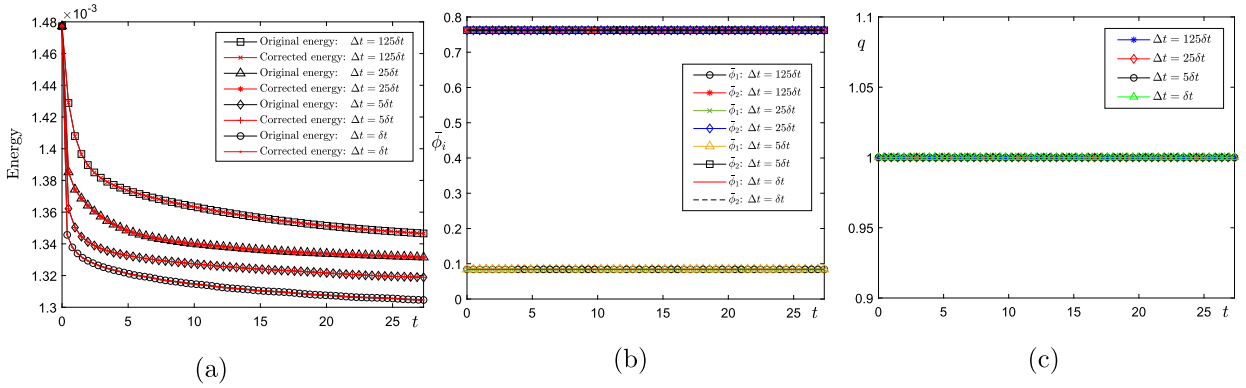

Fig. 5. Evolutions of discrete energy curves (a), average concentration $\bar{\phi}_i$ (b), and auxiliary variable q (c).

Based on the same initial setting and parameters, we next investigate the evolutions of discrete original energy E_o^n and discrete corrected energy E_c^n under different time steps. Fig. 4 shows the snapshots at different moments with $\delta t = 0.5h$. With time evolution, it can be observed that the droplet shrinks and the numerical contact angle approximately becomes 120.8°. The velocity field evolves under the effect of surface tension. Fig. 5(a), (b), and (c) plot the time evolutions of energy curves, average concentration $\bar{\phi}_i$, and auxiliary variable q under different time steps, i.e., $\Delta t = 125\delta t$, $25\delta t$, $5\delta t$, and δt. We can see that the original energy and corrected energy are non-increasing and highly consistent. The average concentrations are conserved and the values of q are consistent with the exact value 1. The computational test results demonstrate that the proposed method not only satisfies the energy dissipation law but also maintains consistency.

4.2. Droplet in contact with solid substrate

In this subsection, we investigate the evolutional dynamics of a single droplet in contact with flat and tilted substrates. The mesh size is $h = 1/64$ (i.e., 256×128 grids). We use $\Delta t = 0.25h$, $Pe = We = Re = 1$, $S = 2$, and $\epsilon = 0.015$ (almost 8 grids in diffuse interface) in all simulations. The initial conditions on $\Omega = (0, 4) \times (0, 2)$ are defined to be

$$\phi_0(x, y, 0) = 0.5 + 0.5 \tanh\left(\frac{0.15 - y}{\sqrt{2}\epsilon}\right), \text{ for flat substrate,} \tag{4.4}$$

$$\phi_0(x, y, 0) = 0.5 + 0.5 \tanh\left(\frac{0.075x - y}{\sqrt{2}\epsilon}\right), \text{ for tilted substrate,} \tag{4.5}$$

$$\phi_1(x, y, 0) = (1 - \phi_0(x, y, 0))\left(\frac{0.8 - \sqrt{(x - 0.2)^2 + (y - 0.15)^2}}{\sqrt{2}\epsilon}\right), \tag{4.6}$$

$$\phi_2(x, y, 0) = 1 - \phi_0(x, y, 0) - \phi_1(x, y, 0), \tag{4.7}$$

$$u(x, y, 0) = v(x, y, 0) = p(x, y, 0) = 0. \tag{4.8}$$

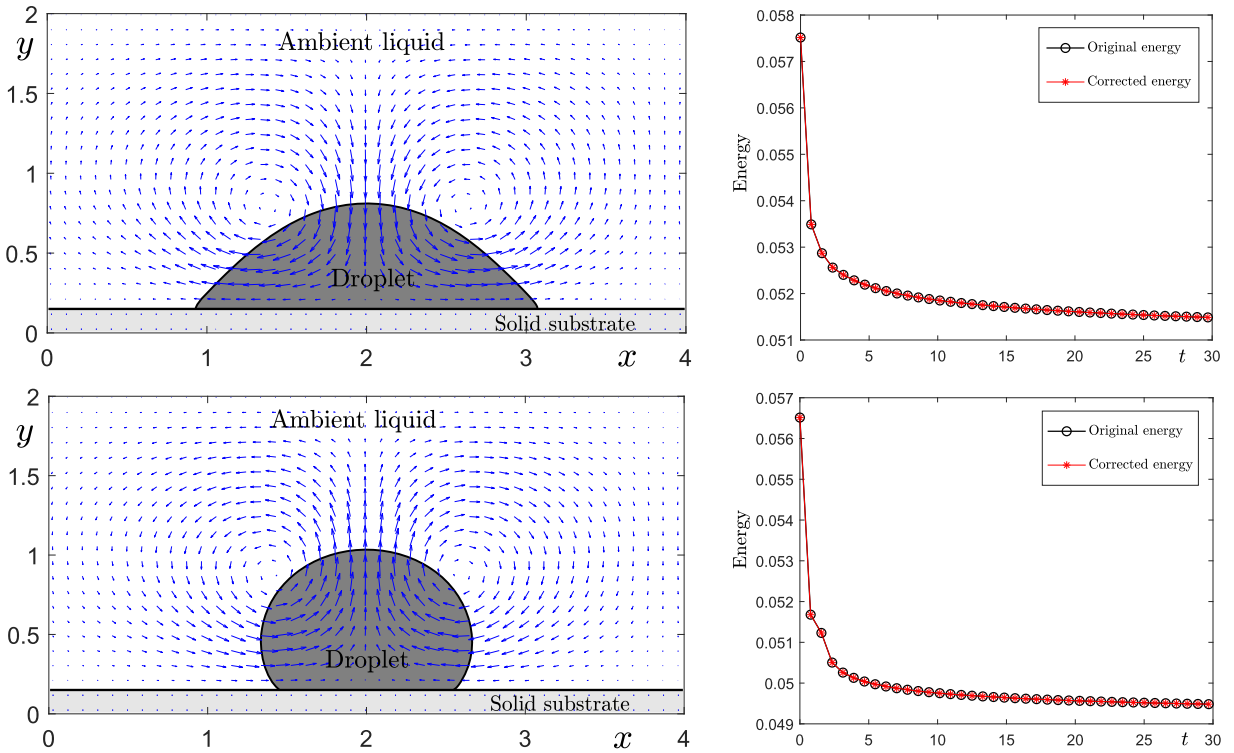

Fig. 6. Single droplet in contact with a flat substrate. The top and bottom rows show the snapshots and energy curves with respect to $\theta = 45°$ and 135°, respectively.

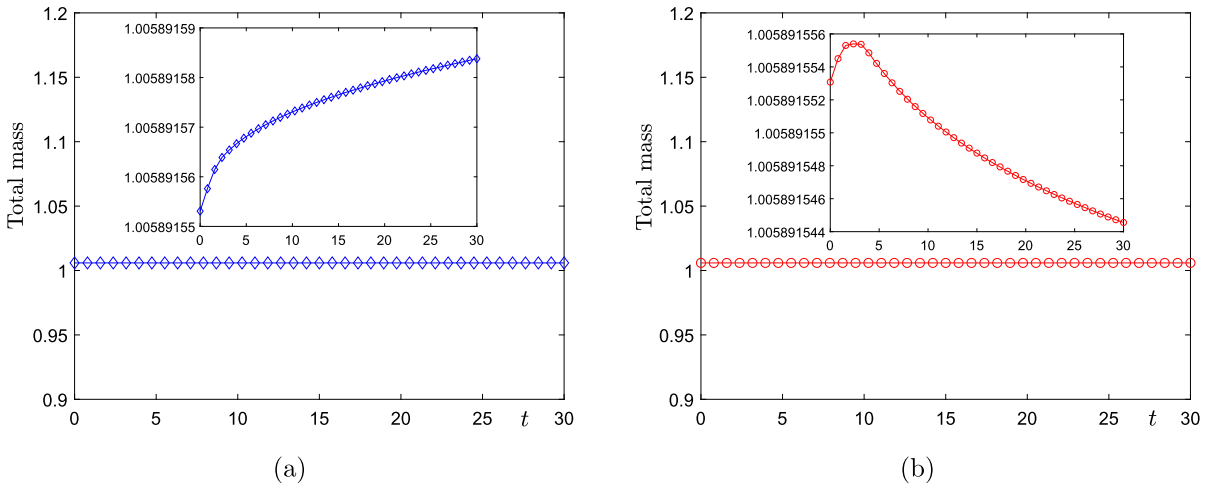

Fig. 7. Evolutions of $\int_\Omega \phi_1 \, d\mathbf{x}$ with respect to (a) $\theta = 45°$ and (b) $\theta = 135°$ on a flat substrate.

The same boundary conditions in previous subsection are used. The top row of Fig. 6 displays the snapshot on a flat substrate at $t = 29.68$ and the energy curves with respect to $\theta = 45°$. The bottom row of Fig. 6 shows the corresponding results with respect to $\theta = 135°$. Under the effect of contact angle, the different wetting phenomena of a single droplet in contact with flat substrate are observed. The circulation of velocity field moves upward and downward with respect to the hydrophobic and hydrophilic behaviors of droplet. During these processes, it can be observed that the original and corrected energies are non-increasing and highly consistent. Fig. 7(a) and (b) show the evolutions of $\int_\Omega \phi_1 \, d\mathbf{x}$ with respect to $\theta = 45°$ and 135°, respectively. In each figure, the inset displays the close-up view within a relatively smaller range. The results indicate that the mass is conserved.

The top and bottom rows of Fig. 8 show the snapshots and energy curves of a single droplet in contact with a tilted substrate with respect to $\theta = 45°$ and 135°, respectively. It can be observed that the hydrophobic and hydrophilic behaviors

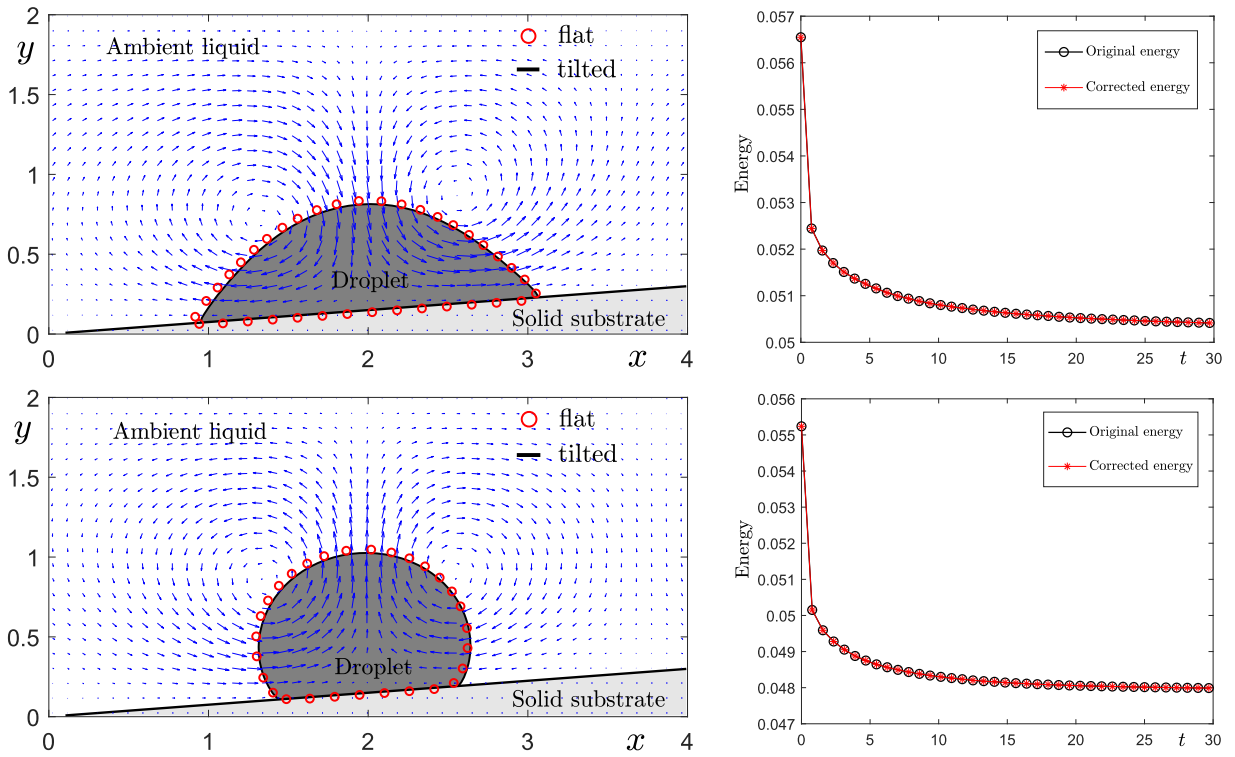

Fig. 8. Single droplet in contact with a tilted substrate. The top and bottom rows show the snapshots and energy curves with respect to $\theta = 45°$ and 135°, respectively.

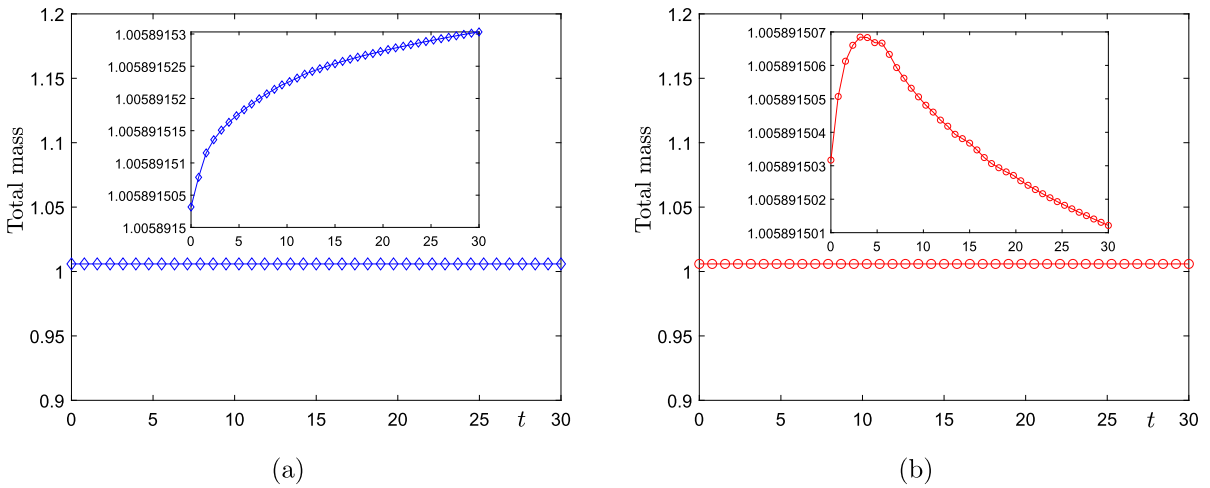

Fig. 9. Evolutions of $\int_\Omega \phi_1 \, d\mathbf{x}$ with respect to (a) $\theta = 45°$ and (b) $\theta = 135°$ on a tilted substrate.

of droplet are similar with the cases on a flat substrate. To perform qualitative comparisons, we rotate the profiles of droplet on a flat substrate in a specific angle and plot them in Fig. 8 with red open circle markers. The computational results confirm that the proposed model can achieve similar wetting phenomena on flat and tilted substrates. On a tilted substrate, the evolution of droplet still dissipates the total energy. In Fig. 9(a) and (b), time evolutions of $\int_\Omega \phi_1 \, d\mathbf{x}$ with respect to $\theta = 45°$ and 135° are plotted. The computational results demonstrate that the fluid preserves the total mass.

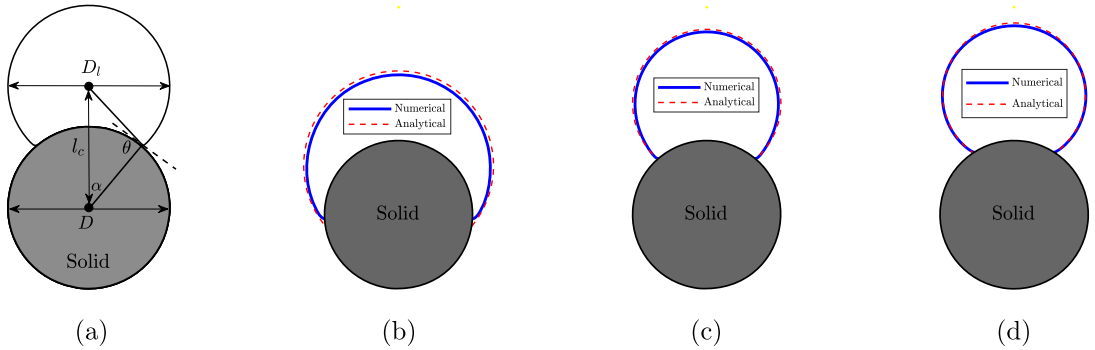

Fig. 10. Comparison of the droplet shapes on a cylinder. Here, (b), (c), and (d) show the results with respect to $\theta = 30°$, $90^c irc$, and $120°$. The analytical and numerical profiles are represented by the blue solid line and the red dashed line, respectively.

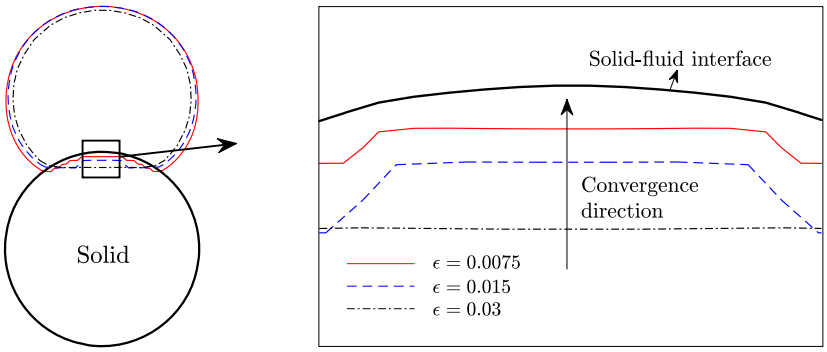

Fig. 11. Convergence of droplet profile with respect to different mesh sizes and ϵ. The right one is the close-up view.

4.3. Droplet on a cylinder and mesh convergence

In the absence of gravity, the final shape of a droplet on a cylinder can be analytically obtained, see [22,43,44]. For a 2D droplet with area A and a static contact angle θ on a cylinder with diameter D (see Fig. 10(a)), the distance between the center of cylinder and the centroid of droplet (l_c) and the diameter of droplet (D_l) can be computed by

$$A = (\alpha + \theta)(D_l/2)^2 - \alpha(D/2) + (D_l D/4)\sin\theta, \tag{4.9}$$

$$D_l = D\cos\theta + \sqrt{D^2\cos^2\theta - D^2 + 4l_c^2}, \tag{4.10}$$

where

$$\alpha = \arccos\left(\frac{D^2 + 4l_c^2 - D_l^2}{4Dl_c}\right).$$

In this test, the full domain is $\Omega = (0, 2.5) \times (0, 2.5)$. The initial state is shown in Fig. 10(a), the parameters are $\Delta t = 0.04$, $h = 2.5/128$ (i.e., 128×128 grids), $\epsilon = 0.0141$ (almost 6 grids in diffuse interface), $Re = Pe = We = 1$. The initial velocities and pressure are zero. The density-matched case is considered. Fig. 10(b), (c), and (d) show the numerical and analytical shapes with respect to $\theta = 30°$, $90°$, and $120°$. It can be observed that the numerical simulations match well with the analytical results.

The phase-field method approximates the solid-fluid boundary with a diffuse region with finite thickness. The diffuse thickness is controlled by the interfacial parameter ϵ. In [43], Liu and Ding observed that the diffuse region between fluid and solid converges as the refinement of grid or ϵ. To show the convergence with respect to mesh and ϵ, we perform the simulations with same initial condition in Fig. 10(a). The contact angle is set to be $60°$. Fig. 11 displays the profiles of droplet with respect to ϵ_h. Here, $\epsilon_h = 0.8405h$ and $h = 2.6/32$, $2.6/64$, and $2.5/128$. It can be observed that the overlap between solid and fluid becomes narrow and the droplet profile converges as the refinement of mesh and ϵ. When the mesh is not enough, the CH dynamics leads to the obvious shrink of local area of droplet. This has been reported in a recent study of Lee et al. [45] and we also observe this phenomenon in present test. To fix this weakness, one can modify the CH model by adding an interfacial correction technique [46], we will investigate this in a separate work.

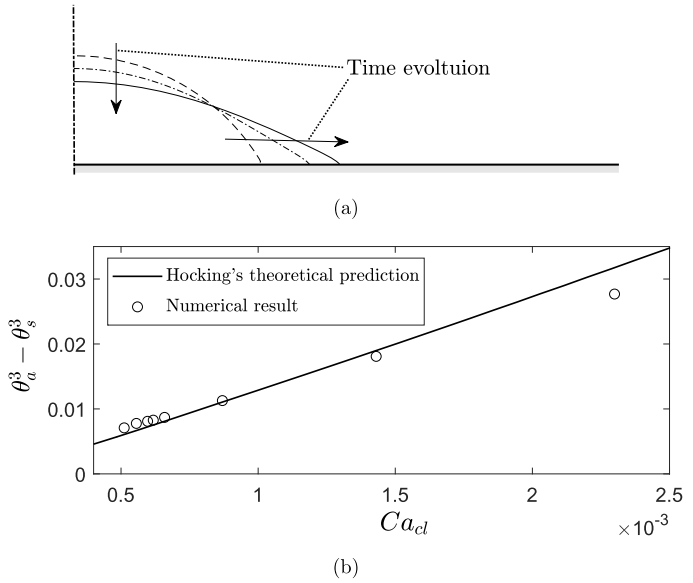

Fig. 12. Droplet spreading on a flat substrate. Here, (a) shows the snapshots of droplet at different moments; (b) plots the analytical and numerical values of $\theta_a^3 - \theta_s^3$.

4.4. Contact line dynamics

In this subsection, we examine the performance of our model in simulating the dynamics of contact line on a flat substrate. During the droplet spreading, Hocking's theory [47] showed that the apparent contact angel θ_a was predicted by the following formula

$$\theta_a^3 = \theta_s^3 + 9Ca_{cl}\ln(R(t)\theta_s/(6e\xi)), \tag{4.11}$$

where θ_s is the target contact angle, $R(t)$ is the instantaneous length of contact line, Ca_{cl} is the instantaneous capillary number and is defined as $Ca_{cl} = \eta U_{cl}/\sigma$, where η is the dynamic viscosity, σ is the surface tension coefficient. The instantaneous velocity can be calculated by

$$U_{cl} = (R(t^{n+1}) - R(t^n))/(t^{n+1} - t^n).$$

Ding and Spelt [48] and Liu and Ding [43] numerically investigated this dynamics with their characteristic moving contact line models. We perform the simulation in a 2D full domain $\Omega = (0, 5) \times (0, 1.25)$. The solid locates under $y = 0.15$. The initial droplet locates on the substrate with initial contact angle 60°. We set $\Delta t = 0.1$, $h = 5/512$ (i.e., 512×128 grids), $\epsilon = 0.0094$ (almost 8 grids in diffuse interface), $Pe = 10$, $Re = 10$, $\xi = 0.0042$, and $\theta_s = 20°$. The top and bottom rows of Fig. 12 show the axisymmetric evolution of droplet profile and the comparison between Hocking's theory predication and the numerical result. With the decrease of Ca_{cl}, the droplet approaches the equilibrium state, and the length of contact line also converges to the equilibrium value. As reported in [43], it is reasonable to expect that $\theta_a^3 - \theta_s^3$ should be proportional to Ca_{cl} at low Ca_{cl}. The present simulation also shows that the computational and analytical results are in good agreement at low Ca_{cl}.

4.5. Flow-coupled phase separation in complex region

The wavy curved channel is a typical irregular domain with complex geometrical shapes. In this subsection, we aim to investigate the fluid flow-coupled phase separation dynamics in the wavy channel. The full computational domain is $\Omega = (0, 4) \times (0, 1)$. The fluid region (i.e., $1 - \phi_0$) has the upper bound $u(x)$ and lower bound $l(x)$ as follows

$$u(x) = 0.05\sqrt{x}\sin(3\pi x) + 0.75, \quad l(x) = 0.01x^2\cos(2\pi x) - 0.04\sin(6\pi x) + 0.3.$$

The initial velocities are zero. The initial states of phase-field function is $\phi_i = 0.5 + 0.1\text{rand}(x, y)$, where $i = 1, 2$ and $\text{rand}(x, y)$ is the random value between -1 and 1. Along x-direction, we consider the zero Neumann boundary condition for ϕ_i. The parameters are set to be $h = 1/128$ (i.e., 512×128 grids), $\Delta t = 0.001$, $\epsilon = 0.0038$ (almost 4 grids in diffuse interface), $S = 2$, $Pe = We = Re = 1$, and $\theta = 90°$. The evolutional snapshots are shown in Fig. 13 in which the velocity field is represented by the blue arrows. Fig. 14(a) displays the evolutions of original energy and corrected energy. We can see that the energy curves are decreasing and highly consistent. To show the merit of the correction technique, we also plot

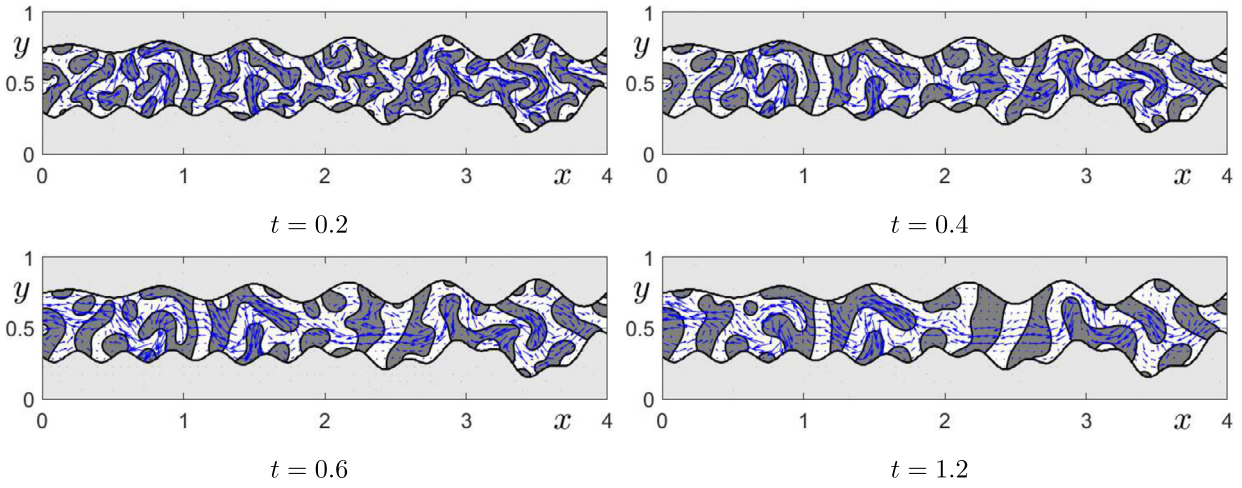

Fig. 13. Fluid flow-coupled binary phase separation in a wavy curved channel. The computational moments are shown under each figure.

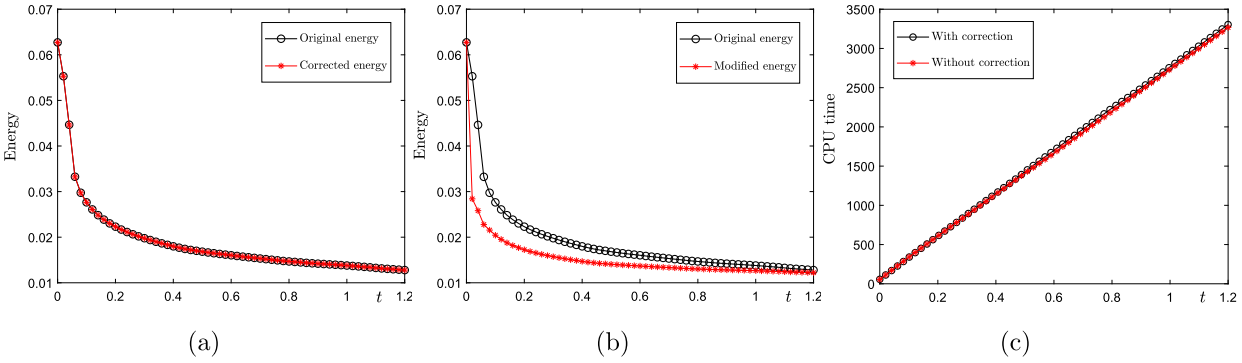

Fig. 14. Original energy and corrected energy are shown in (a); Original energy and modified energy are shown in (b); CPU costs are plotted in (c).

the energy curves in Fig. 14(b) in which the original SAV approach (without correction) is used to perform the calculation. We find that the consistency is lost because of the difference between the original and modified energies. In Fig. 14(c), the CPU times (in second) consumed by the SAV approach with and without correction are shown. It can be observed that the correction technique does not obviously increase the computational costs.

4.6. Cavity flow with solid obstacles

If q equal to its exact value 1, the numerical method in Section 3 will be an appropriate approximation of incompressible NS equations. On the contrary, the consistency between the numerical method and original model will be violated. To improve the consistency, we propose a correction technique for the auxiliary variable q in Section 3 and we validate this via the lid-driven cavity flow in the domain with solid obstacles. The computational domain is $\Omega = (0, 2) \times (0, 0.5)$. The parameters are $h = 1/128$ (i.e., 256×64 grids), $\Delta t = 0.002$, $Re = 2400$. The lid velocity on the upper boundary is $\overline{U} = 1$. On other boundaries, the velocity field is no-slip. For convenience, we only solve the fluid equations in this test. The top row of Fig. 15 shows the steady state of velocities and the inset is the local close-up view. Due to the distribution of four solid obstacles, the velocities in regions I, II, III, and IV are obviously different. In region I, the effect of shear force and the existence of solid lead to the formation of circulation. In region II, the circulation with smaller magnitude appears between the bigger and smaller obstacles. In region III, the circulation is not obvious because the distance between two obstacles are so close that the velocity field can not fully evolve. In region IV, the magnitude of velocity field is negligible because the incoming flow from right side is hindered and then is attracted to the upper position by shear force. In the bottom row of Fig. 15, we plot the evolutions of auxiliary variable q with respect to the original SAV approach (without correction) and the present method (with correction). We can see that the original SAV approach causes q gradually deviates away from the exact value 1 in time, while the present method leads to highly consistent result.

To test the choice of κ, we perform the same simulation with different values of κ ($\kappa = 10^{-4}, 10^{-6}, 10^{-8}$, and 10^{-10}). For the fluid-structure interaction with stationary solids, we hope the magnitude of velocity in solid becomes small enough. In Table 1, the values of $\min(\sqrt{u^2 + v^2})$ in solid phase are listed. As the refinement of κ, we find that the magnitude of

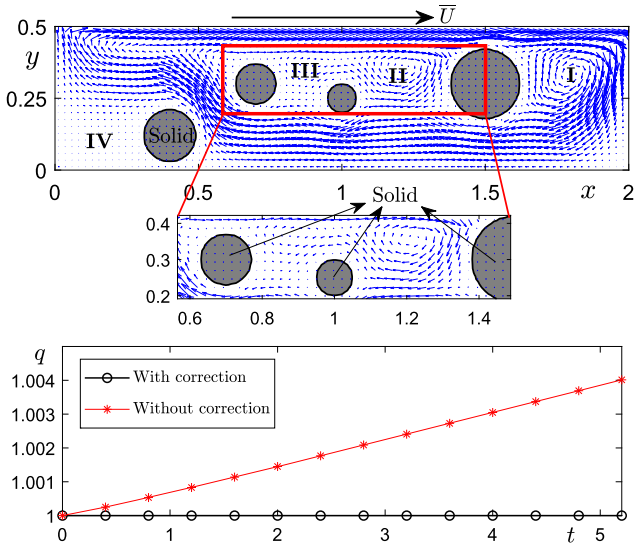

Fig. 15. Lid-driven cavity flow in the domain with solid obstacles. The bottom row displays the evolutions of auxiliary variable q with respect to original SAV approach and the present method.

Table 1
Values of $\min(\sqrt{u^2+v^2})$ with respect to different κ.

κ	10^{-4}	10^{-6}	10^{-8}	10^{-10}
$\min(\sqrt{u^2+v^2})$	3.386e-7	6.120e-9	6.411e-10	4.499e-10

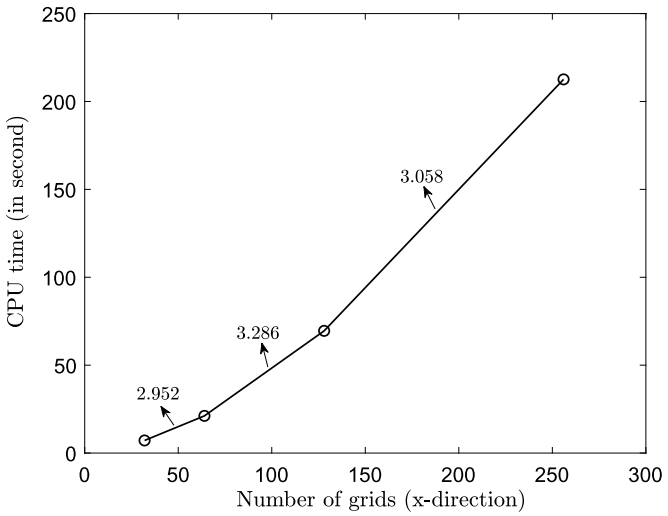

Fig. 16. CPU costs (in second) with respect to different mesh sizes.

velocity becomes smaller. Since the results with respect to $\kappa = 10^{-8}$ and 10^{-10} are small enough and in same order, we simply choose $\kappa = 10^{-8}$ in this work.

In this work, the space is discretized with the FDM. The fully discrete scheme and the implementation have been described in subsection 3.4. In each time step, we need to solve Poisson-type equations with variable coefficients to update the intermediate velocities. The pressure Poisson equation is solved with a linear multigrid algorithm [49]. Therefore, the whole cost of computational time is of $O(N\log(N))$, where N represents the total number of grids in computational domain. We perform the same simulation with aforementioned parameters. In Fig. 16, the CPU costs (in second) with respect to different mesh sizes are listed. As we can observe, the relation between CPU cost and mesh size is almost linear.

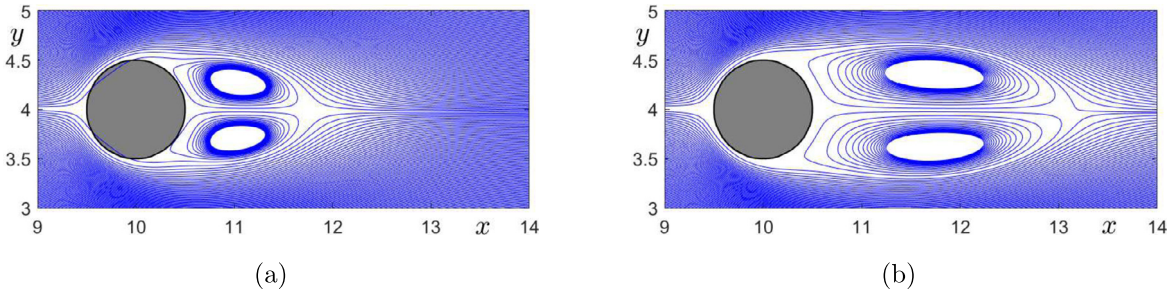

Fig. 17. Flow past a stationary circular cylinder at (a) $Re = 20$ and (b) $Re = 40$.

Table 2
Wake length for flow past a stationary circular cylinder at $Re = 20$ and $Re = 40$.

Authors	Xu and Wang [53]	Wang et al. [50]	Russell and Wang [54]	Silva et al. [55]	Present
$Re = 20$	0.92	0.978	0.94	1.04	1.15
$Re = 40$	2.21	2.35	2.35	2.55	2.51

4.7. Flow past a stationary circular cylinder

Flow past a stationary circular cylinder is a typical benchmark in fluid-structure interaction. Many researchers considered this test to verify the performance of immersed boundary method (IBM) [50,51] and penalty-type method [30,52]. In the present simulation, the full domain is $\Omega = (0, 32) \times (0, 8)$. A circular cylinder with radius 0.5 locates at $(10, 4)$. The parameters are set to be $\Delta t = 2h^2$ and $h = 1/16$ (i.e., 512×128 grids). Since we only consider the single phase flow, the Pe and We are absent. We first consider the flow past a stationary circular cylinder at low Reynolds number ($Re = 20$ and 40). The inlet velocity and diameter of cylinder are used as characteristic velocity and characteristic length, respectively. Fig. 17(a) and (b) show the stream lines at $Re = 20$ and 40. The present wake lengths and previous results are listed in Table 2. It is worth noting that the penalty method cannot strictly guarantee that the stream line does not penetrate the solid phase, slight non-physical penetration in Fig. 17(a) can be observed. To fix this problem, the boundary condition-enforced IBM [51] will be a good choice. However, present simulation indicate that the penetration does not obviously affect the wake length, the present and previous results are quantitatively similar.

At moderate Reynolds number, the flow past a circular cylinder becomes unstable and forms the well-known Karman vortex street. In this test, the dimensionless drag coefficient is defined by

$$C_d = \frac{F_d}{(1/2)\rho U_\infty^2 D},$$

where F_d is the drag force and it can be calculated by following [56], D is the diameter of cylinder, U_∞ is the inlet velocity. We set $Re = 100$ and display the snapshots of vorticity at different moments in Fig. 18. We observe the vortex shedding occurs periodically. In Table 3, the drag coefficients are listed. The present and previous results are quantitatively similar.

4.8. Binary fluid dynamics in 3D domain

Herein, we first consider the fluid flow-coupled phase separation in 3D wavy channel. The parameters are defined as $\Delta t = 0.001$, $Pe = We = Re = 1$, $\epsilon = 0.0075$ (almost 4 grids in diffuse interface), $S = 2$, $h = 1/64$ (i.e., $128 \times 64 \times 64$ grids), and $\theta = 90°$. The initial conditions on $\Omega = (0, 2) \times (0, 1) \times (0, 1)$ are as follows

$$\phi_0(x, y, z, 0) = 0.5 + 0.5 \tanh\left(\frac{\sqrt{(y-0.5)^2 + (z-0.5)^2}}{\sqrt{2}\epsilon} - \frac{(0.01x^2\cos(2\pi x) - 0.04\sin(4\pi x) + 0.3)(0.95 - 0.4\cos(\vartheta + \pi x))}{\sqrt{2}\epsilon}\right), \tag{4.12}$$

$$\phi_1(x, y, z, 0) = (1 - \phi_0(x, y, z, 0))(0.5 + 0.5\mathrm{rand}(x, y, z)), \tag{4.13}$$

$$\phi_2(x, y, z, 0) = 1 - \phi_0(x, y, z, 0) - \phi_1(x, y, z, 0), \tag{4.14}$$

$$u(x, y, z, 0) = v(x, y, z, 0) = w(x, y, z, 0) = p(x, y, z, 0) = 0, \tag{4.15}$$

where $\vartheta = \tan^{-1}((y - 0.5)/(z - 0.5))$ if $z > 0.5$ and $\vartheta = \pi + \tan^{-1}((y - 0.5)/(z - 0.5))$ otherwise. Fig. 19 shows the binary phase separations at different moments. Here, the light yellow region is the interior of irregular domain and green profile

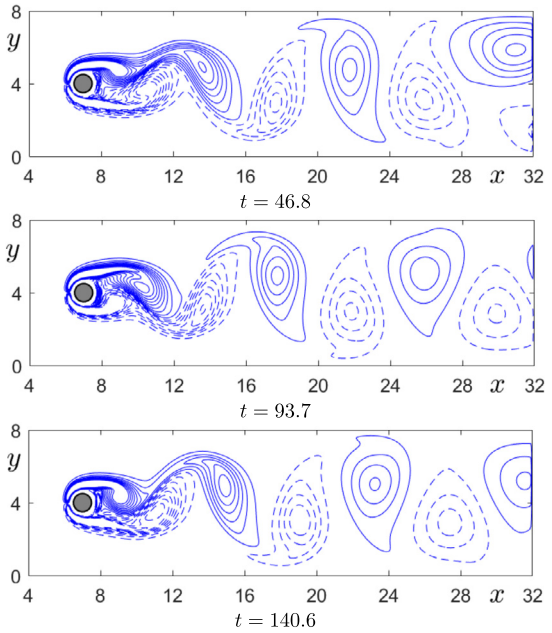

Fig. 18. Flow past a stationary circular cylinder at $Re = 100$. Under each snapshot of vorticity, the computational moments are shown.

Table 3
Drag coefficients of flow past a circular cylinder at $Re = 100$.

Authors	Mittal et al. [57]	Hendersen [58]	Braza et al. [59]	Bergmann et al. [30]	Present
$Re = 100$	1.35	1.35	1.36	1.41	1.37

represents the fluid-fluid interface (i.e., $\phi_1 = 0.5$). Fig. 20 displays the evolutions of energy curves and auxiliary variable q, we find that the original energy and corrected energy are consistently decreasing, q is consistent with the exact value 1.

Next, we investigate the motion and deformation of a single droplet in a flexed channel. The computational domain is $\Omega = (0, 4) \times (0, 2) \times (0, 2)$. Along x-direction, the left side and right side are inlet and outlet, respectively. The inlet velocity is fixed as 0.04. The radius of the initial droplet is 0.3 and its center locates at $(1, 1, 0.65)$. The parameters are defined as $\Delta t = 1/32$ (i.e., $128 \times 64 \times 64$ grids), $\epsilon = 0.015$ (almost 4 grids in diffuse interface), $Pe = 0.2/\epsilon$, $We = 0.65$, $Re = 20$, $S = 2$. Fig. 21 shows the snapshots at different moments and we can observe the deformations of droplet at different positions of channel. From the result plotted in Fig. 22, we find q is still consistent with 1.

4.9. Falling droplet in contact with obstacles

Finally, we validate the performance of our proposed model and numerical method by simulating the falling droplet in contact with solids. For convenience, we assume the density ratio between two fluids are small. For a single phase flow, the temperature-induced density difference is comparatively small relative to the bulk phase, the well-known Boussinasq approximation can be used to treat the buoyancy term. In this test, we assume the density ratio between two fluids are small. Although the present problem does not belong to Boussinasq approximation, the similar idea is adopted to rewrite the momentum equation into

$$\rho_* \left(\frac{\partial \mathbf{u}}{\partial t} + \mathbf{u} \cdot \nabla \mathbf{u} \right) = -\nabla p + \frac{1}{Re} \Delta \mathbf{u} - \sum_{i=1}^{2} \phi_i \nabla \mu_i + (\rho(\phi_1, \phi_2) - \rho_*)\mathbf{g}, \tag{4.16}$$

where $\rho(\phi_1, \phi_2) = \rho_1 \phi_1 + \rho_2 \phi_2$ is the density, ρ_1 and ρ_2 are positive constants, ρ_* is the background density. In 2D space, $\mathbf{g} = (0, -g)$ is the gravity. In the present simulation, the domain is $\Omega = (0, 2) \times (0, 4)$. Along x-direction, the pressure and ϕ_i $(i = 1, 2)$ are periodic. The no-slip boundary condition is used for velocities on all boundaries. The initial velocities are zero. The initial droplet with radius: 0.41 locates at $(1, 2.6)$. The solid obstacles are three circles with radii: 0.38, 0.25, 0.25 and central positions: $(1, 1.8)$, $(0.5, 0.85)$, $(1.5, 0.85)$, respectively. The parameters are $\Delta t = h = 1/64$ (i.e., 256×128 grids), $\epsilon = 0.0075$ (almost 4 grids in diffuse interface), $\rho_1 = 3$, $\rho_2 = \rho_* = 1$, $g = 1$, $Pe = We = 1$, $Re = 30$. In Fig. 23, the snapshots with respect to $\theta = 45°$ are displayed. The results with respect to $\theta = 135°$ are shown in Fig. 24. Under different wetting conditions, we observe that the difference only occurs on fluid-solid interface at early stage. In the hydrophilic case, the

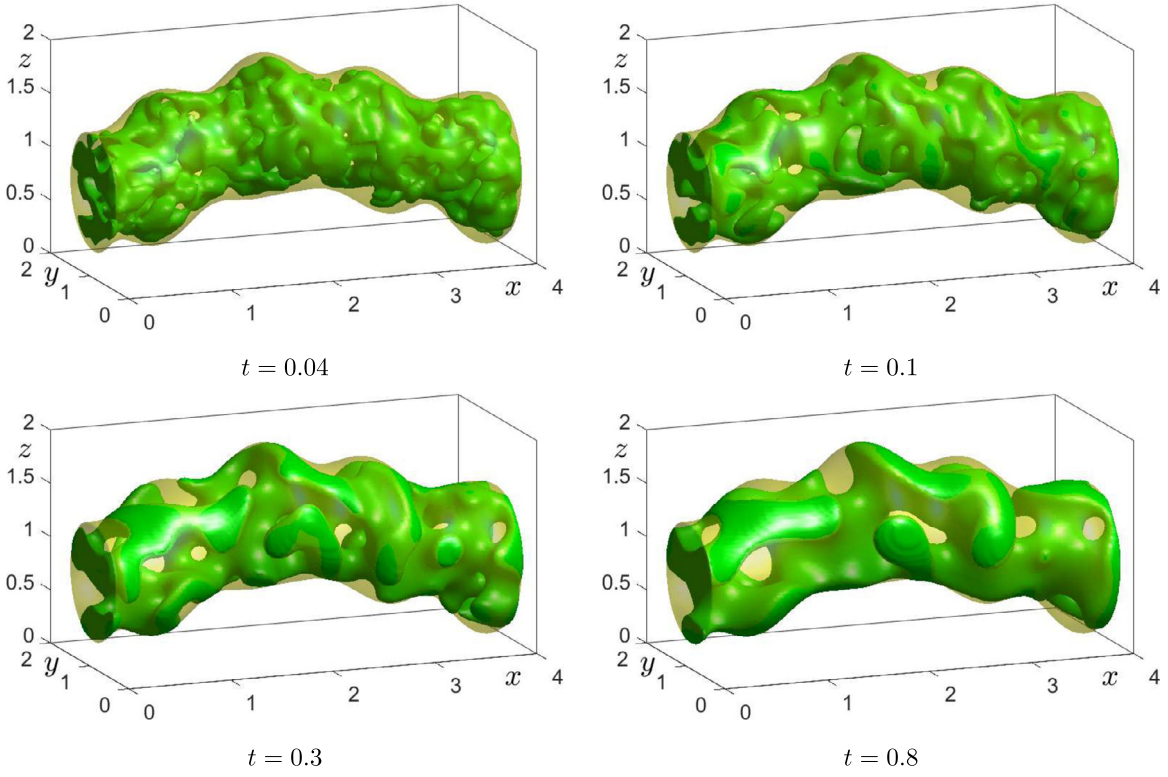

Fig. 19. Fluid flow-coupled binary phase separation in a 3D wavy curved channel. The computational moments are shown under each figure.

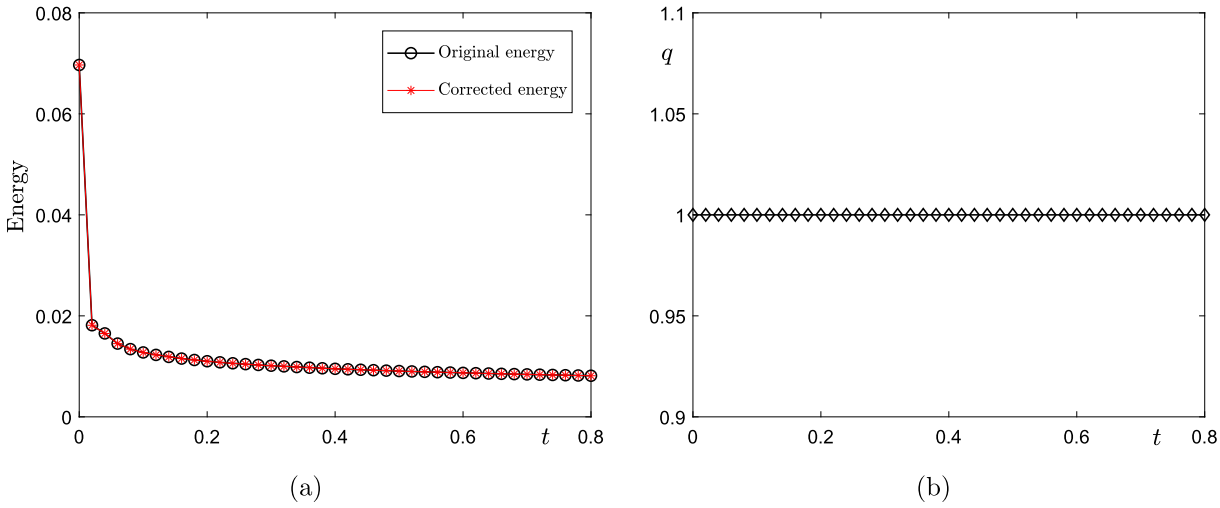

Fig. 20. Evolutions of energy curves in 3D wavy curved channel is shown in (a); Evolution of auxiliary variable q is shown in (b).

droplet are first separated into two smaller droplets and then they merge with each other to form a whole liquid. For the hydrophobic case, the two resulting droplets keep separated all along. The results plotted in Fig. 25 indicate that q and its exact value 1 are highly consistent. We plot the time evolutions of $\int_\Omega \phi_1 \, d\mathbf{x}$ with respect to $\theta = 45°$ and $135°$ in Fig. 26(a) and (b), respectively. The results indicate that the mass of fluid is conserved.

4.10. Kelvin–Helmholtz instability with different Reynolds numbers

The difference of velocity in fluid field leads to the formation of vortex structure, this is the famous Kelvin–Helmholtz instability (KHI). In atmospheric sciences, the KHI describes the formation of billowing cloud at lower atmosphere [60]. To

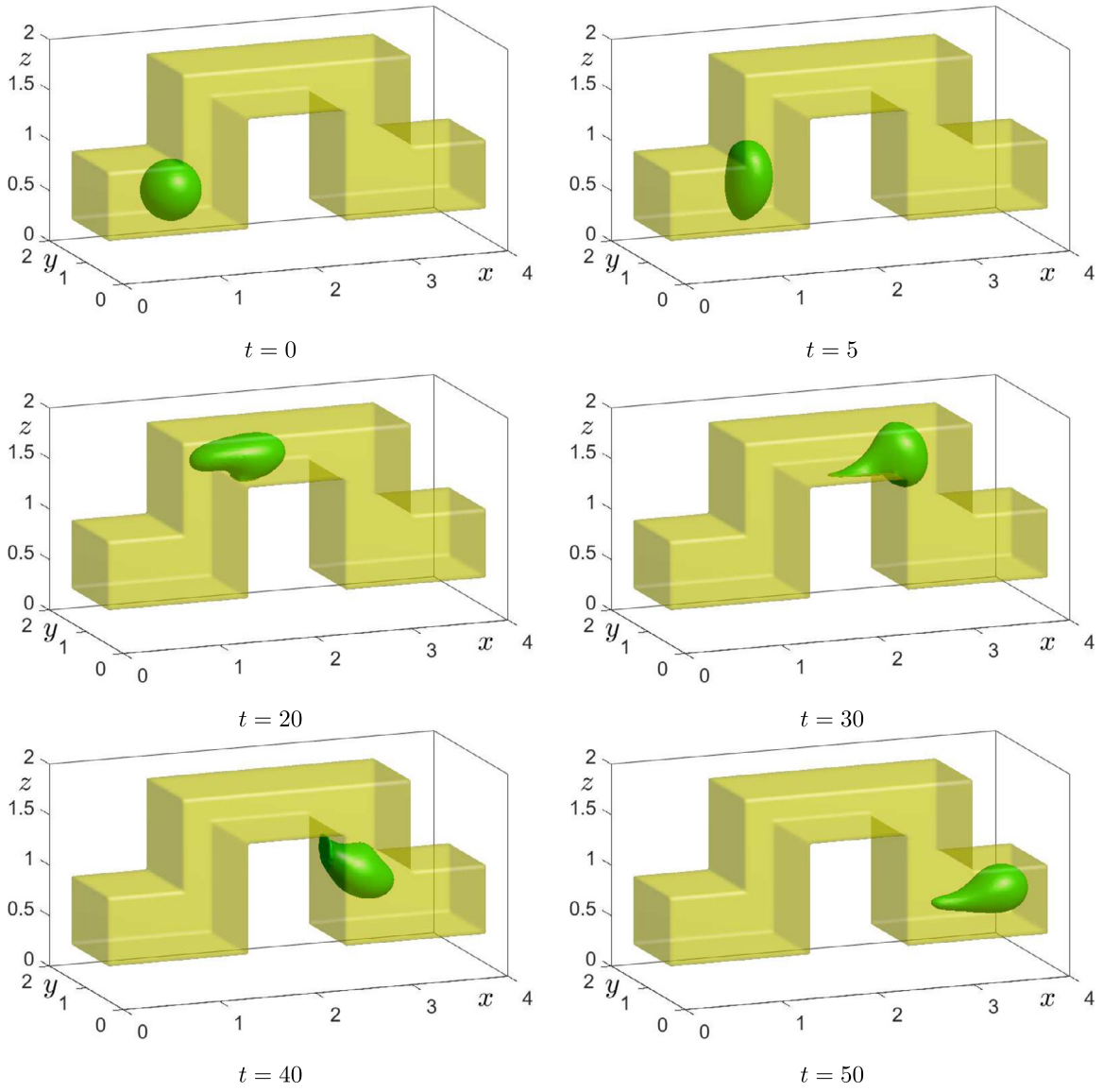

Fig. 21. Motion and deformation of a single droplet in a flexed channel. The computational moments are shown under each figure.

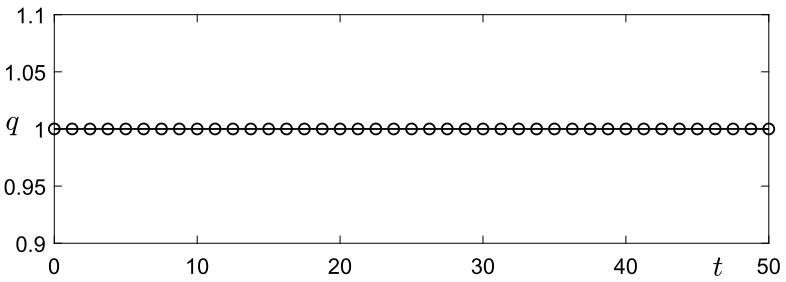

Fig. 22. Time evolutions of auxiliary variable q with respect to the droplet motion in a flexed channel.

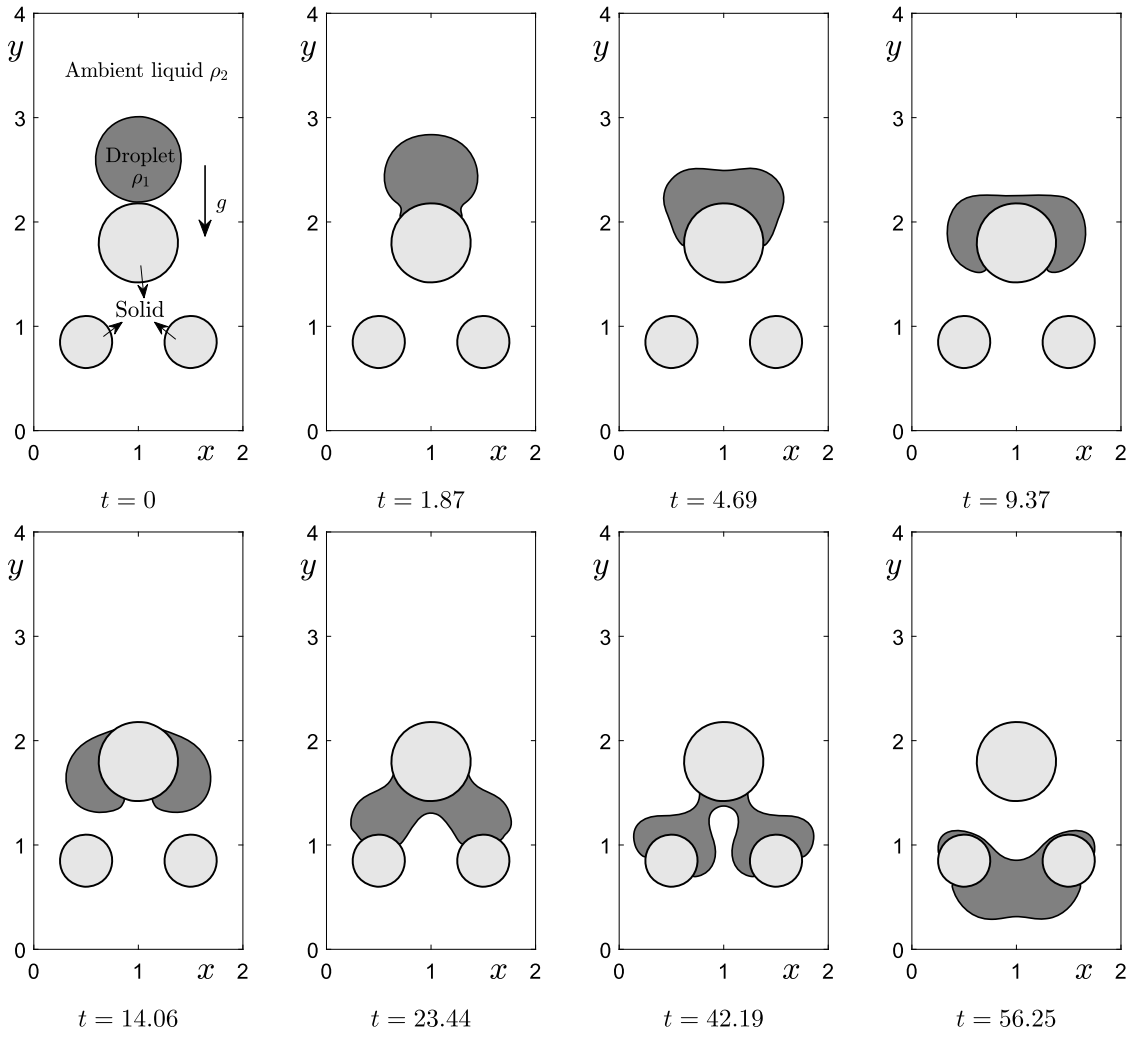

Fig. 23. Falling droplet in contact with obstacles under $\theta = 45°$. The computational moments are shown under each figure.

test our method at different Reynolds numbers, we herein simulate the two-phase KHI with a solid plate embedding in domain. The initial conditions are defined as

$$\phi_0(x, y) = \begin{cases} 1 & \text{if } 0.48 \le x \le 0.52 \text{ and } 0.2 \le y \le 0.8, \\ 0 & \text{otherwise.} \end{cases} \tag{4.17}$$

$$\phi_1(x, y, 0) = (1 - \phi_0(x, y)) \left[\frac{1}{2} + \frac{1}{2} \tanh \left(\frac{y - 0.5 - 0.01 \sin(8\pi x)}{\sqrt{2}\epsilon} \right) \right], \tag{4.18}$$

$$\phi_2(x, y, 0) = 1 - \phi_0(x, y) - \phi_1(x, y, 0), \tag{4.19}$$

$$u(x, y, 0) = U \tanh \left(\frac{y - 0.5 - 0.01 \sin(8\pi x)}{\sqrt{2}\epsilon} \right), \tag{4.20}$$

$$v(x, y, 0) = 0, \quad p(x, y, 0) = 0. \tag{4.21}$$

Here, $U = 0.2$ is used. The schematic illustration of initial setting is shown in Fig. 27. The simulations are performed in $\Omega = (0, 1) \times (0, 1)$. The parameters are set to be $\Delta t = 0.001$, $h = 1/128$ (i.e., 128×128 grids), $\epsilon = 0.0038$ (almost 4 grids in diffuse interface), $Pe = 0.1/\epsilon$, and $\theta = 150°$. The surface tension is absent. The density ratio is $1 : 1$. The top, middle, and bottom rows of Fig. 28 show the snapshots with respect to $Re = 10$, 10^3, and 10^6, respectively. With the increase of Reynolds number, the fluid instability evolves fast. This simulation indicates that our method can work at a relatively large Reynolds number (i.e., $Re = 10^6$). The time evolutions of total mass under different Reynolds numbers are shown in Fig. 29. The inset displays the close-up view in a smaller range. It can be seen that the mass of fluid is conserved even if a large Reynolds number ($Re = 10^6$) is used.

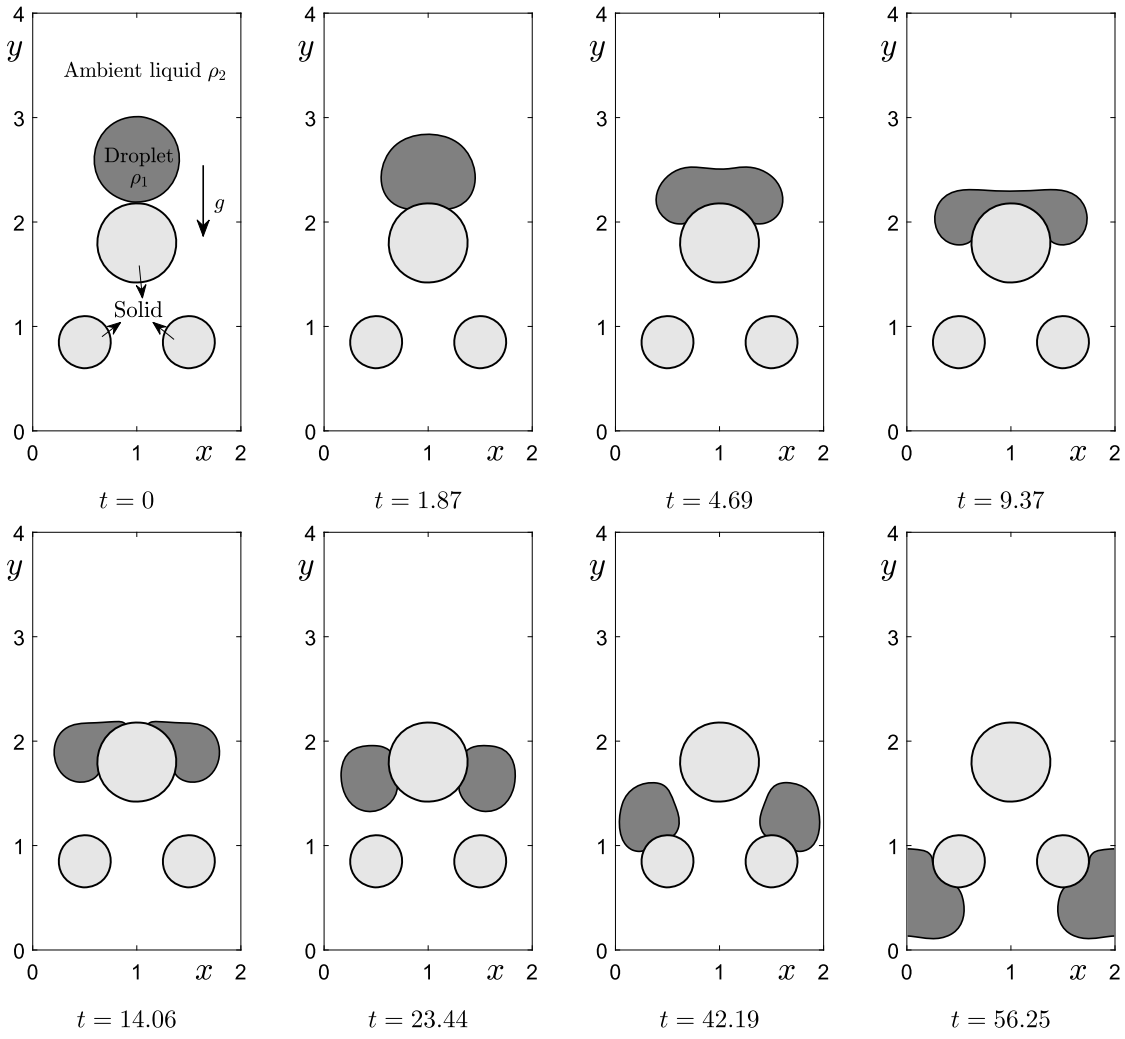

Fig. 24. Falling droplet in contact with obstacles under $\theta = 135°$. The computational moments are shown under each figure.

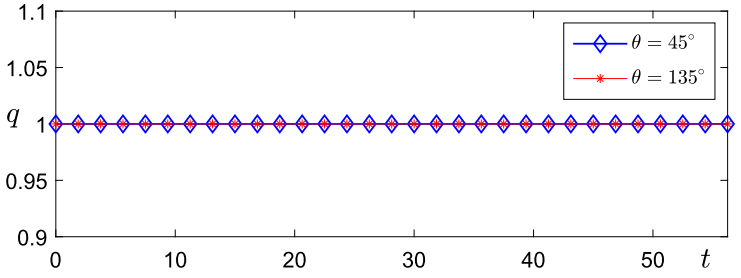

Fig. 25. Time evolutions of auxiliary variables with respect to the falling droplet in contact with obstacles.

4.11. Droplet impacting with variable density and viscosity ratios

To construct energy-stable scheme, the SAV-type method is adopted in this work. It is worth noting that SAV method is hard to treat the fluid problems with variable density and viscosity ratios. To show the capability of our proposed diffuse interface model in simulating droplet impacting with variable density and viscosity ratios, we herein do not use the SAV scheme to compute the following NS equations with variable density and viscosity [61]

$$\rho(\boldsymbol{\phi})\left(\frac{\partial \mathbf{u}}{\partial t} + \mathbf{u}\cdot\nabla\mathbf{u}\right) = -\nabla p + \frac{1}{Re}\nabla\cdot\eta(\boldsymbol{\phi})(\nabla\mathbf{u} + \nabla\mathbf{u}^T) + \mathbf{SF}, \tag{4.22}$$

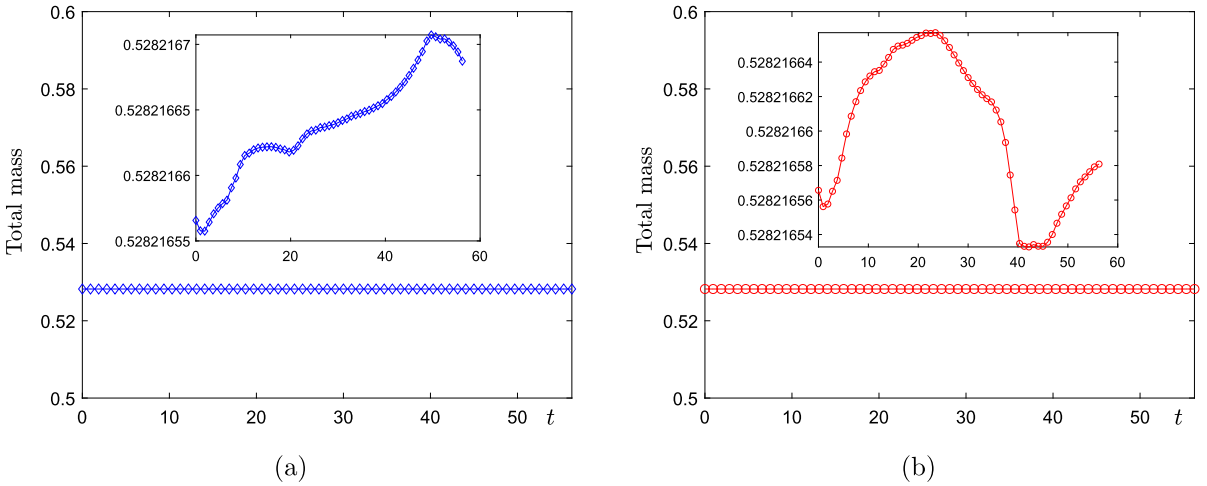

Fig. 26. Evolutions of $\int_\Omega \phi_1 \, d\mathbf{x}$ with respect to (a) $\theta = 45°$ and (b) $\theta = 135°$. The insets display the close-up views in a relatively small range.

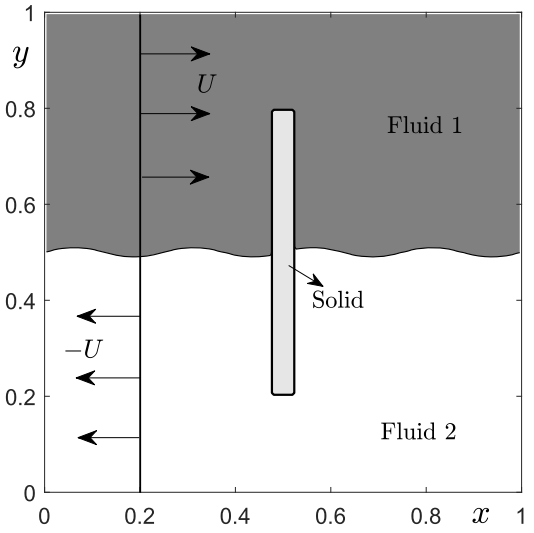

Fig. 27. Initial setting of two-phase KHI in contact with a solid plate.

$$\nabla \cdot \mathbf{u} = 0, \tag{4.23}$$

where $\rho(\boldsymbol{\phi}) = \rho_1\phi_1 + \rho_2\phi_2$ and $\eta(\boldsymbol{\phi}) = \eta^1\phi_1 + \eta^2\phi_2$, **SF** represents the surface tension. The pressure Poisson equation with variable coefficients is directly computed. Please refer to [62] for the numerical treatment. In this test, the full domain is $\Omega = (0, 3.5) \times (0, 3.5)$. The parameters are $\Delta t = 8h^2$, $h = 3.5/128$ (i.e., 128×128 grids), $\epsilon = 0.013$ (almost 4 grids in diffuse interface), $Pe = 1/\epsilon$, $Re = 650$, $We = 8$, $\theta = 90°$. The densities are $\rho_1 = 829$ and $\rho_2 = 55.16$. The viscosities are $\eta^1 = 40$ and $\eta^2 = 1$. These parameters are chosen to match the setting in [63]. Here, the effect of gravity is neglected. The top and middle rows in Fig. 30 show the experimental results in [64] and numerical results in [63]. The bottom row displays the present results. The present and previous computational results are qualitatively similar. This simulation indicates that our proposed phase-field model has the potential capability to treat two-phase flows with variable density and viscosity ratios in contact with solid. In our upcoming work, an accurate and stable scheme for treating the problems with large density and viscosity ratios will be investigated.

5. Concluding remarks

In this work, we developed a diffuse interface-type model for describing incompressible binary fluid flows in arbitrary domains. The modified ternary CH system with wetting term was derived to capture the fluid-fluid interface and reflect the contact angle phenomenon. The NS equations with penalty term was used to update the velocities in the domains with solid obstacles. Since the solid region is fixed, we analytically proved that the proposed model satisfied the energy

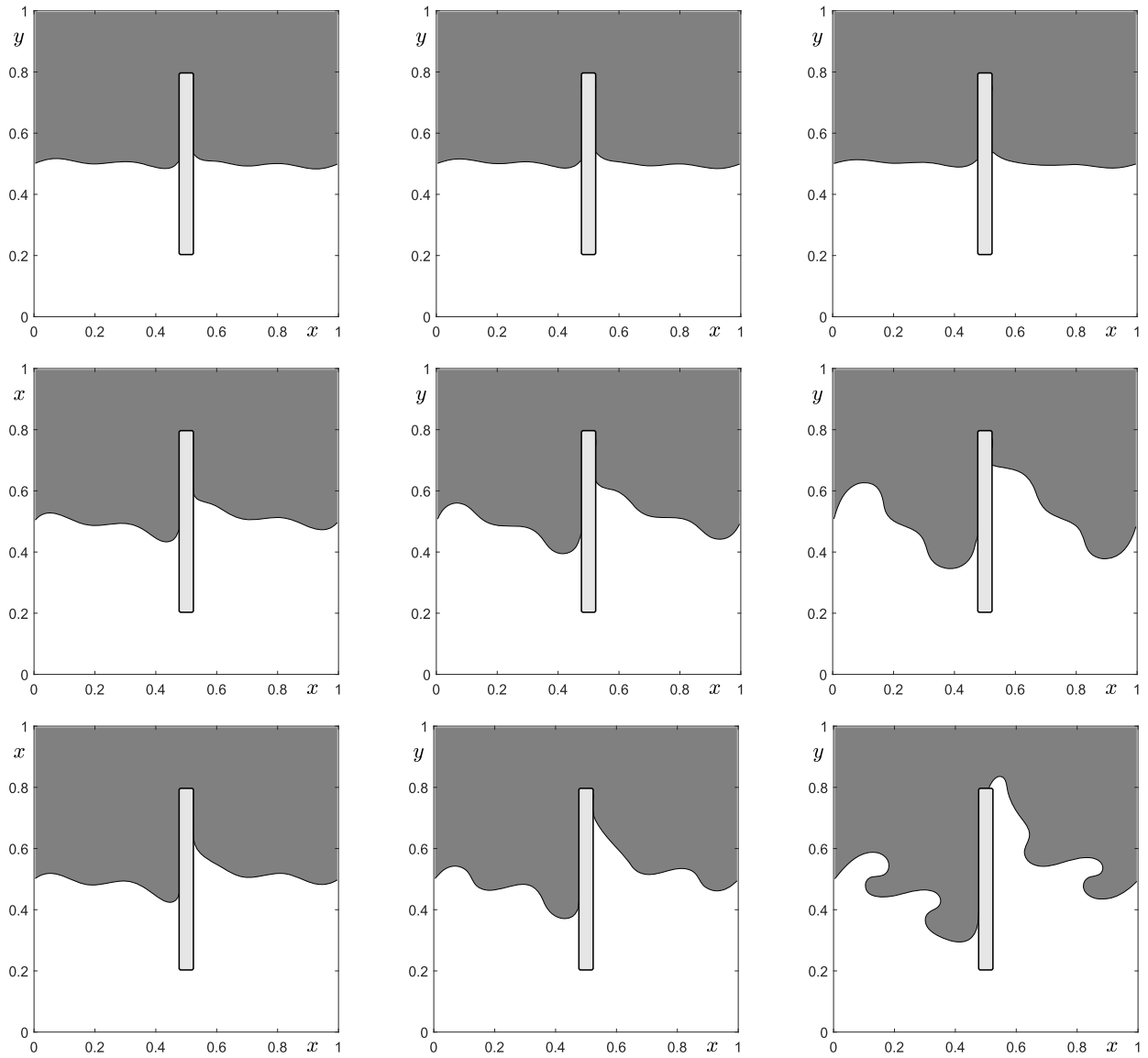

Fig. 28. Snapshots of two-phase KHI with respect to different Reynolds numbers. The top, middle, and bottom rows correspond to $Re = 10$, 10^3, and 10^6, respectively. From left to right, the results are at $t = 0.3$, 0.6, 1.2.

dissipation property. By utilizing the SAV method with correction techniques, the second-order accurate, linear, and energy-stable numerical scheme was proposed. The time-discretized energy dissipation law was estimated. The proposed model was efficient to implement because all decoupled computations were performed on regular Cartesian grids without complicated boundary treatment. The numerical simulations indicated the accuracy, stability, and capability of our proposed method. In upcoming works, the proposed method will be extended for the heat convection-coupled incompressible fluids [65,66] in irregular domains.

CRediT authorship contribution statement

Junxiang Yang: Formal analysis, Investigation, Methodology, Software, Supervision, Validation, Visualization, Writing – original draft, Writing – review & editing. **Zhijun Tan:** Methodology, Software, Supervision, Validation, Visualization, Writing – review & editing. **Jian Wang:** Validation, Visualization, Writing – review & editing. **Junseok Kim:** Formal analysis, Investigation, Methodology, Software, Supervision, Validation, Visualization, Writing – original draft, Writing – review & editing.

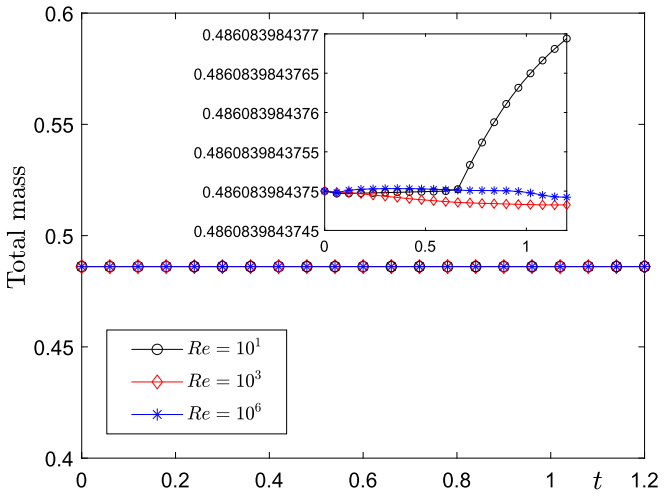

Fig. 29. Time evolutions of $\int_\Omega \phi_1 \, d\mathbf{x}$ under different Reynolds numbers.

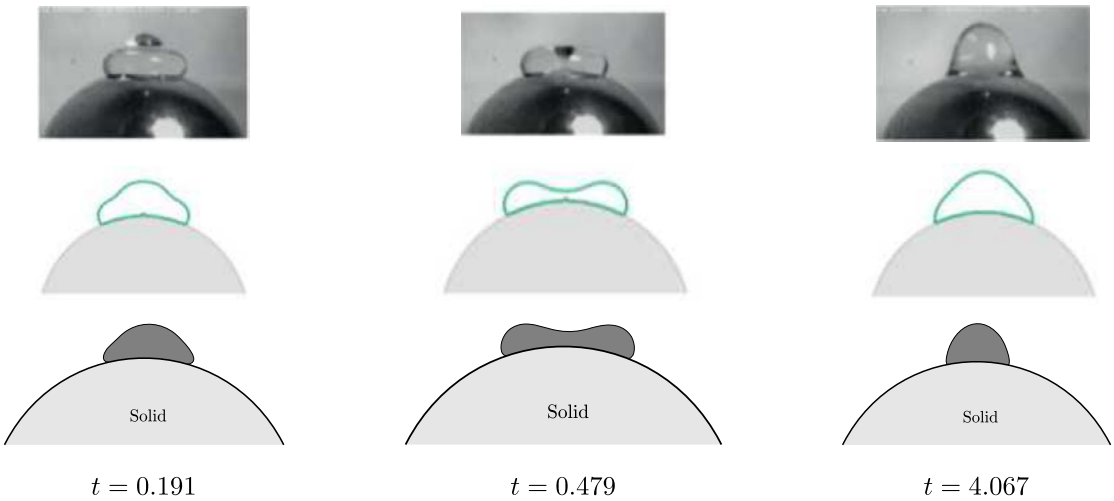

Fig. 30. Snapshots of the droplet shape during the droplet impact on a solid. The experimental results and numerical results are adapted from [64] and [63] with the permissions of Elsevier and American Institute of Physics, respectively. The bottom row displays the present simulation.

Declaration of competing interest

The authors declare that they have no known competing financial interests or personal relationships that could have appeared to influence the work reported in this paper.

Data availability

Data will be made available on request.

Acknowledgement

J. Yang is supported by the National Natural Science Foundation of China (No. 12201657), the China Postdoctoral Science Foundation (No. 2022M713639), and the 2022 International Postdoctoral Exchange Fellowship Program (Talent-Introduction Program) (No. YJ20220221). Jian Wang expresses thanks for The Startup Foundation for Introducing Talent of NUIST, and Jiangsu shuangchuang project (JSSCBS20210473). Z. Tan is supported by the National Nature Science Foundation of China (11971502), Guangdong Natural Science Foundation (2022A1515010426), Guangdong Province Key Laboratory of Computational Science at the Sun Yat-sen University (2020B1212060032), and Key-Area Research and Development Program of Guangdong Province (2021B0101190003). The corresponding author (J.S. Kim) was supported by the National Research

Foundation of Korea (NRF) grant funded by the Korea government (MSIT) (No. 2022R1A2C1003844). The authors thank the reviewers for their constructive comments on this revision.

References

[1] K. Mu, C. Zhang, T. Si, H. Ding, Experimental and numerical investigations on characteristics of coaxial liquid cone in coflow focusing, Phys. Rev. Fluids 7 (2022) 024001.
[2] K. Mu, R. Qiao, T. Si, X. Cheng, H. Ding, Interfacial instability and transition of jetting and dripping modes in a co-flow focusing process, Phys. Fluids 33 (2021) 052118.
[3] N. Valizadeh, T. Rabczuk, Isogeometric analysis of hydrodynamics of vesicles using a monolithic phase-field approach, Comput. Methods Appl. Mech. Eng. 388 (2022) 114191.
[4] J. Yang, Y. Li, J. Kim, Totally decoupled implicit-explicit linear scheme with corrected energy dissipation law for the phase-field fluid vesicle model, Comput. Methods Appl. Mech. Eng. 399 (2022) 115330.
[5] B. Shen, B. Riviere, A sequential discontinuous Galerkin method for two-phase flow in deformable porous media, Comput. Methods Appl. Mech. Eng. 399 (2022) 115266.
[6] X. Zheng, K. Zhao, T. Jackson, J. Lowengrub, Tumor growth towards lower extracellular matrix conductivity regions under Darcy's Law and steady morphology, J. Math. Biol. 85 (2022) 5.
[7] L. Chen, J. Zhao, A novel second-order linear scheme for the Cahn–Hilliard–Navier–Stokes equations, J. Comput. Phys. 423 (2020) 109782.
[8] J. Zhao, D. Han, Second-order decoupled energy-stable schemes for Cahn–Hilliard–Navier–Stokes equations, J. Comput. Phys. 443 (2021) 110536.
[9] Q. Xia, Q. Yu, Y. Li, A second-order accurate, unconditionally energy stable numerical scheme for binary fluid flows on arbitrarily curved surfaces, Comput. Methods Appl. Mech. Eng. 384 (2021) 113987.
[10] Z. Guo, P. Lin, J. Lowengrub, S. Wise, Mass conservative and energy stable finite difference methods for the quasi-incompressible Navier–Stokes–Cahn–Hilliard system: promitive variable and projection-type schemes, Comput. Methods Appl. Mech. Eng. 326 (2017) 144–174.
[11] J.W. Cahn, J.E. Hilliard, Free energy of a nonuniform system. I. Interfacial free energy, J. Chem. Phys. 28 (2) (1958) 258–267.
[12] S. Lee, J. Shin, Energy stable compact scheme for Cahn–Hilliard equation with periodic boundary condition, Comput. Math. Appl. 77 (1) (2019) 189–198.
[13] W. Chen, W. Feng, Y. Liu, C. Wang, S. Wise, A second order energy stable scheme for the Cahn–Hilliard–Hele–Shaw equation, Discrete Contin. Dyn. Syst., Ser. B 24 (2019) 149–182.
[14] X. Li, Z. Qiao, C. Wang, Stabilization parameter analysis of a second-order linear numerical scheme for the nonlocal Cahn–Hilliard equation, IMA J. Numer. Anal. (2022), https://doi.org/10.1093/imanum/drab109.
[15] X. Li, Z. Qiao, C. Wang, Double stabilizations and convergence analysis of a second-order linear numerical scheme for the nonlocal Cahn–Hilliard equation, Sci. China Math. 65 (2022), https://doi.org/10.1007/s11425-016-5135-4.
[16] Y. Gong, J. Zhao, Q. Wang, Arbitrarily high-order linear energy stable schemes for gradient flow models, J. Comput. Phys. 419 (2020) 109610.
[17] Z. Liu, X. Li, A highly efficient and accurate exponential semi-implicit scalar auxiliary variable (ESI-SAV) approach for dissipative system, J. Comput. Phys. 447 (2021) 110703.
[18] N. Jiang, H. Yang, SAV decoupled ensemble algorithms for fast computation of Stokes–Darcy flow ensembles, Comput. Methods Appl. Mech. Eng. 387 (2021) 114150.
[19] X. Li, L. Ju, X. Meng, Convergence analysis of exponential time differencing schemes for the Cahn–Hilliard equation, Commun. Comput. Phys. 26 (5) (2019) 1510–1529.
[20] L. Luo, X-P. Wang, X-C. Cai, An efficient finite element method for simulation of droplet spreading on a topologically rough surface, J. Comput. Phys. 349 (2017) 233–252.
[21] Y. Li, J-I. Choi, J. Kim, Multi-component Cahn–Hilliard system with different boundary conditions in complex domains, J. Comput. Phys. 323 (2016) 1–16.
[22] Z. Guo, F. Yu, P. Lin, S.M. Wise, J. Lowengrub, A diffuse domain method for two-phase flows with large density ratio in complex geometries, J. Fluid Mech. 907 (2021) A38.
[23] J. Yang, J. Wang, J. Kim, Energy-stable method for the Cahn–Hilliard equation in arbitrary domains, Int. J. Mech. Sci. 228 (2022) 107489.
[24] J. Kim, Phase field computations for ternary fluid flows, Comput. Methods Appl. Mech. Eng. 196 (2007) 4779–4788.
[25] H-R. Liu, P. Gao, H. Ding, Fluid-structure interaction involving dynamic wetting: 2D modeling and simulations, J. Comput. Phys. 348 (2017) 45–65.
[26] H.G. Lee, J. Kim, Buoyancy-driven mixing of multi-component fluids in two-dimensional tilted channels, Eur. J. Mech. B, Fluids 42 (2013) 37–46.
[27] C-Y. Zhang, H. Ding, P. Gao, Y-L. Wu, Diffuse interface simulation of ternary fluids in contact with solid, J. Comput. Phys. 309 (2016) 37–51.
[28] J-J. Huang, Hybrid lattice-Boltzmann finite-difference simulation of ternary fluids near immersed solid objects of general shapes, Phys. Fluids 33 (2021) 072105.
[29] H. Liang, B.C. Shi, Z.H. Chai, Lattice Boltzmann modeling of three-phase incompressible flows, Phys. Rev. E 93 (2016) 013308.
[30] M. Bergmann, J. Hovnanian, A. Iollo, An accurate cartesian method for incompressible flows with moving boundaries, Commun. Comput. Phys. 15 (2014) 1266–1290.
[31] G. Zhu, H. Chen, J. Yao, S. Sun, Efficiet energy-stable schemes for the hydrodynamics coupled phase-field model, Appl. Math. Model. 70 (2019) 82–108.
[32] J. Yang, Z. Tan, J. Kim, Linear and fully decoupled scheme for a hydrodynamics coupled phase-field surfactant system based on a multiple auxiliary variables approach, J. Comput. Phys. 452 (2022) 110909.
[33] J. Shen, J. Xu, J. Yang, The scalar auxiliary variable (SAV) approach for gradient flows, J. Comput. Phys. 353 (2018) 407–416.
[34] L. Lin, Z. Yang, S. Dong, Numerical approximation of incompressible Navier–Stokes equations based on an auxiliary energy variable, J. Comput. Phys. 388 (2019) 1–22.
[35] Q. Ye, Z. Ouyang, C. Chen, X. Yang, Efficient decoupled second-order numerical scheme for the flow-coupled Cahn–Hilliard phase-field model of two-phase flows, J. Comput. Appl. Math. 405 (2022) 113875.
[36] C. Chen, X. Yang, A second-order time accurate and fully-decoupled numerical scheme of the Darcy–Newtonian–Nematic model for two-phase complex fluids confined in the Hele–Shaw cell, J. Comput. Phys. 456 (2022) 111026.
[37] J-W. Choi, H.G. Lee, D. Jeong, J. Kim, An unconditionally gradient stable numerical method for solving the Allen–Cahn equation, Physica A 388 (2009) 1791–1803.
[38] M. Jiang, Z. Zhang, J. Zhao, Improving the accuracy and consistency of the scalar auxiliary variable (SAV) method with relaxation, J. Comput. Phys. 456 (2022) 110954.
[39] N. Ni, Z. Yang, S. Dong, Energy-stable boundary conditions based on a quadratic form: applications to outflow/open-boundary problems in incompressible flows, J. Comput. Phys. 391 (2019) 179–215.
[40] F.H. Harlow, J.E. Welch, Numerical calculation of time-dependent viscous incompressible flow of fluid with free surface, Phys. Fluids 8 (1965) 2182–2189.
[41] Y. Chen, J. Shen, Efficient, adaptive energy stable schemes for the incompressible Cahn–Hilliard Navier–Stokes phase-field models, J. Comput. Phys. 308 (2016) 40–56.

[42] G. Zhu, H. Chen, A. Li, S. Sun, J. Yao, Fully discrete energy stable scheme for a phase-field moving contact line model with variable densities and viscosities, Appl. Math. Model. 83 (2020) 614–639.
[43] H-R. Liu, H. Ding, A diffuse-interface immersed-boundary method for two-dimensional simulation of flows with moving contact lines on curved substrates, J. Comput. Phys. 294 (2015) 484–502.
[44] X. Liu, Z. Chai, C. Zhan, B. Shi, W. Zhang, A diffuse-domain phase-field lattice Boltzmann method for two-phase flows in complex geometries, Multiscale Model. Simul. 20 (4) (2022) 1411–1436.
[45] H.G. Lee, J. Yang, J. Park, J. Kim, Effect of space dimension on the equilibrium solutions of the Cahn–Hilliard and conservatice Allen–Cahn equations, Numer. Math., Theory Methods Appl. 13 (3) (2020) 644–664.
[46] Q. Xia, J. Kim, Y. Li, Modeling and simulation of multi-component immiscible flows based on a modified Cahn–Hilliard equation, Eur. J. Mech. B, Fluids 97 (2022) 194–204.
[47] L.M. Hocking, The spreading of a thin drop by gravity and capillary, Q. J. Mech. Appl. Math. 36 (1983) 55–69.
[48] H. Ding, P.D.M. Spelt, Wetting condition in diffuse interface simulations of contact line condition, Phys. Rev. E 75 (2007) 046708.
[49] C. Lee, D. Jeong, J. Shin, Y. Li, J. Kim, A fourth-order spatial accurate and practically stable compact scheme for the Cahn–Hilliard equation, Physica A 409 (2014) 17–28.
[50] Z. Wang, J. Fan, K. Cen, Immersed boundary method for the simulation of 2D viscous flow based on vorticity-velocity formulations, J. Comput. Phys. 228 (2009) 1504–1520.
[51] W.W. Ren, C. Shu, J. Wu, W.M. Yang, Boundary condition-enforced immersed boundary method for thermal flow problems with Dirichlet temperature condition and its applications, Comput. Fluids 57 (2012) 40–51.
[52] D.Z. Noor, M-J. Chern, T-L. Horng, An immersed boundary method to solve fluid-solid interaction problems, Comput. Mech. 44 (2009) 447–453.
[53] S. Xu, Z.J. Wang, An immersed interface method for simulating the interaction of a fluid with moving boundaries, J. Comput. Phys. 216 (2006) 454–493.
[54] D. Russell, Z.J. Wang, A cartesian grid method for modeling multiple moving objects in 2D incompressible viscous flow, J. Comput. Phys. 191 (2003) 177–205.
[55] A.L.F.L.E. Silva, A. Silveira-Neto, J.J.R. Damasceno, Numerical simulation of two-dimensional flows over a circular cylinder using the immersed boundary method, J. Comput. Phys. 189 (2003) 351–370.
[56] M-C. Lai, C.S. Peskin, An immersed boundary method with formal second-order accuracy and reduced numerical viscosity, J. Comput. Phys. 160 (2000) 705–719.
[57] R. Mittal, H. Dong, M. Bozkurttas, F. Najjar, A. Vargas, A. von Loebbecke, A versatile sharp interface immersed boundary method for incompressible flows with complex boundaries, J. Comput. Phys. 227 (2008) 4825–4852.
[58] R. Henderson, Details of the drag curve near the onset of vortex shedding, Phys. Fluids 7 (1995) 2102–2104.
[59] M. Braza, P. Chassaing, H.H. Minh, Numerical study and physical analysis of the pressure and velocity fields in the near wake of a circular cylinder, J. Fluid Mech. 165 (1986).
[60] H.G. Lee, J. Kim, Two-dimensional Kelvin–Helmholtz instabilities of multi-component fluids, Eur. J. Mech. B, Fluids 49 (2015) 77–88.
[61] H-R. Liu, C.S. Ng, K.L. Chong, D. Lohse, R. Verzicco, An efficient phase-field method for turbulent multiphase flows, J. Comput. Phys. 446 (2021) 110659.
[62] H.G. Lee, J. Kim, On the long time simulation of the Rayleigh–Taylor instability, Int. J. Numer. Methods Eng. 85 (2011) 1633–1647.
[63] J-J. Huang, L. Zhang, Simplified method for wetting on curved boundaries in conservative phase-field lattice-Boltzmann simulation of two-phase flows with large density ratios, Phys. Fluids 34 (2022) 082101.
[64] S. Mitra, M.J. Sathe, E. Doroodchi, R. Utikar, M.K. Shah, V. Pareek, J.B. Joshi, G.M. Evans, Droplet impact dynamics on a spherical particle, Chem. Eng. Sci. 100 (2013) 105–119.
[65] X. Pan, C. Lee, J-I. Choi, Efficient monolithic projection method for time-dependent conjugate heat transfer problems, J. Comput. Phys. 369 (2018) 191–208.
[66] X. Pan, K-H. Kim, J-I. Choi, Monolithic projection-based method with staggered time discretization for solving non-Oberbeck–Boussinesq natural convection flows, J. Comput. Phys. 463 (2022) 111238.